4.2 INVESTIGATION OF SUBGRID-SCALE SCALAR FLUX AND ITS PRODUCTION RATE USING MEASUREMENT DATA (HATS)

Qinglin Chen, Chenning Tong*
Department of Mechanical Engineering
Clemson University, Clemson, South Carolina 29634

1. INTRODUCTION

Large-eddy simulation (LES) computes the large, or resolvable scales of a turbulent flow and models the effects of the small, or subgrid scales (SGS). When the filter scale is in the inertial range, the energy-containing scales are well resolved and most of the turbulent stress is contained in the resolvable scales. The effects of subgrid scales are generally considered to be limited to extracting energy from the resolvable scales at the correct rate (Lilly (1967); Domaradzki *et al.* (1993); Borue and Orszag (1998)). Thus, the LES results are to some extent insensitive to the subgrid-scale model employed (Nieuwstadt and de Valk (1987); Mason (1994)).

However, in LES of high-Reynolds-number turbulent boundary layers, such as the atmospheric boundary layer (ABL), the filter scale in the near-wall region is inevitably in the energy-containing scales (Kaimal *et al.* (1972); Mason (1994); Peltier *et al.* (1996); Tong *et al.* (1998, 1999)). This causes the near-wall results to depend heavily on the SGS model (Tong *et al.* (1999)). Therefore, the deficiencies of SGS models are likely to result in inaccuracies in the LES statistics in the near-wall region. For example, the standard Smagorinsky model overpredicts the mean scalar gradient and the mean scalar variance, but underpredicts the mean vertical scalar flux in the LES of the unstable ABL (Mason and Thomson (1992); Sullivan *et al.* (1994)). Therefore, an important question in improving SGS models is how the SGS turbulence and SGS models affect the resolvable-scale statistics under these conditions.

Previous studies of SGS turbulence have been generally focused on the energy transfer rate from the resolvable to the subgrid scales (e.g., Borue and Orszag (1998); Domaradzki *et al.* (1993)). However, a limitation of such studies is that they do not provide information on how the SGS turbulence affects the resolvable-scale statistics.

Traditionally, SGS models are studied primarily in two ways: *a priori* and *a posteriori* tests (e.g., Clark *et al.* (1979); McMillan and Ferziger (1979); Bardina *et al.* (1980); Nieuwstadt and de Valk (1987); Piomelli *et al.* (1988); Lund and Novikov (1992); Mason and Thomson (1992); Domaradzki *et al.* (1993); Piomelli (1993); Härtel *et al.* (1994); Liu *et al.* (1994); Mason (1994); Meneveau (1994); Peltier *et al.* (1996); Juneja and Brasseur (1999); Sarghini *et al.* (1999); Tao *et al.* (2000); Porté-Agel *et al.* (2001); Sullivan *et al.* (2003)). While these tests have contributed greatly to our understanding of the current SGS models, they also have their limitations. For *a priori* tests, it is difficult to infer the effects of model performance on LES results. For *a posteriori* tests, it is difficult to relate the deficiencies of LES results to specific model behaviors (Chen and Tong (2006)).

To better understand the effects of SGS turbulence and SGS models on the resolvable-scale statistics, an systematic approach was employed (Chen *et al.* (2003, 2005); Chen and Tong (2006)), which uses the transport equations of the resolvable-scale velocity and velocity-scalar joint probability density function (JPDF). The use of the JPDF transport equations has several advantages over traditional methods for testing SGS models. First, it deals with the resolvable-scale statistics, whose accurate predictions are usually the primary objective of LES whereas the instantaneous SGS variables are very difficult interpret. Second, unlike the filtered Navier-Stokes equations and the scalar transport equation, the JPDF transport equation is not chaotic. Therefore, certain analytical results of the equation (Jaberi *et al.* (1996); Sabelnikov (1998)) can be used to understand the behavior of SGS models (Chen and Tong (2006)). The JPDF equations can be used to study the SGS turbulence and to perform both statistical *a priori* and *a posteriori* tests of SGS models. Chen and Tong (2006) emphasized such *a priori* tests provide a strong linkage between the modeled SGS terms and the resolvable-scale velocity JPDF, and therefore, are qualitatively different from the traditional *a priori* tests based on correlations of the measured and modeled SGS variables.

Chen and Tong (2006) used this approach to study the SGS turbulence in the surface layer of the ABL and identified several deficiencies of the SGS models that affects the LES statistics. They argued that the overpredictions of the mean shear and streamwise velocity variance near the surface by the Smagorinsky model are partly due to the under-prediction of the anisotropy of the SGS stress and its variations in the near-wall region. They also pointed out that the under-prediction of the vertical velocity skewness is likely due to the inability of the Smagorinsky model to predict the asymmetry in the production rate of the vertical normal component of the SGS stress. These analyses based on the JPDF equation provide important knowledge for improving SGS model.

The present work studies the influence of the SGS scalar flux and the SGS stress on the resolvable-scale velocity-scalar JPDF using the JPDF transport equa-

*Corresponding author. E-mail: ctong@ces.clemson.edu

tion, which can be derived following the method given by (Pope (2000)). Differentiating the definition of the JPDF:

$$f = \left\langle \delta[\theta^r - \psi] \prod_{i=1}^{3} \delta[u_i^r - v_i] \right\rangle, \quad (1)$$

where δ is the Dirac delta function, and $\mathbf{v}$ and ψ are the sample-space variables for the resolvable-scale velocity $\mathbf{u}^r$ and the resolvable-scale scalar θ^r (a superscript r denotes a resolvable-scale variable), respectively, and the angle brackets denote an ensemble mean, we obtain

$$\frac{\partial f}{\partial t} = -\frac{\partial}{\partial v_i}\left\{\left\langle \frac{\partial u_i^r}{\partial t}|\mathbf{u^r} = \mathbf{v}, \theta^r = \psi \right\rangle f\right\} - \frac{\partial}{\partial \psi}\left\{\left\langle \frac{\partial \theta^r}{\partial t}|\mathbf{u^r} = \mathbf{v}, \theta^r = \psi \right\rangle f\right\}. \quad (2)$$

Substituting the time derivatives, $\frac{\partial u_i^r}{\partial t}$ and $\frac{\partial \theta^r}{\partial t}$, in Eq. (2) with the right-hand side of the equation for the resolvable-scale velocity:

$$\frac{\partial u_i^r}{\partial t} = -\frac{\partial u_j^r u_i^r}{\partial x_j} - \frac{\partial \tau_{ij}}{\partial x_j} - \frac{\partial p^r}{\partial x_i} + \frac{g}{\Theta}\theta^r \delta_{i3} + \nu \frac{\partial^2 u_i^r}{\partial x_j \partial x_j}, \quad (3)$$

where $\tau_{ij} = (u_i u_j)^r - u_i^r u_j^r, p^r$, Θ, θ, and ν are the SGS stress (the Leonard stress $L_{ij} = (u_i^r u_j^r)^r - u_i^r u_j^r$ has been included in τ_{ij}), the filtered pressure, the mean potential temperature, the fluctuation potential temperature, and the kinematic viscosity, respectively, and the filtered resolvable-scale scalar equation:

$$\frac{\partial \theta^r}{\partial t} = -\frac{\partial \theta^r u_i^r}{\partial x_i} - \frac{\partial F_i}{\partial x_i} + \Gamma \frac{\partial^2 \theta^r}{\partial x_i^2}, \quad (4)$$

where $F_i = (u_i\theta)^r - u_i^r\theta^r$ and Γ are the SGS scalar flux and the molecular diffusivity respectively, we have

$$\frac{\partial f}{\partial t} + v_j \frac{\partial f}{\partial x_j} = \frac{\partial}{\partial v_i}\left\{\left\langle \frac{\partial \tau_{ij}}{\partial x_j}|\mathbf{u^r} = \mathbf{v}, \theta^r = \psi \right\rangle f\right\} + \frac{\partial}{\partial v_i}\left\{\left\langle \frac{\partial p^r}{\partial x_i}|\mathbf{u^r} = \mathbf{v}, \theta^r = \psi \right\rangle f\right\} - \frac{g}{\Theta}\frac{\partial}{\partial v_3}\left\{\langle \theta^r|\mathbf{u^r} = \mathbf{v}, \theta^r = \psi \rangle f\right\} + \frac{\partial}{\partial \psi}\left\{\left\langle \frac{\partial F_i}{\partial x_i}|\mathbf{u^r} = \mathbf{v}, \theta^r = \psi \right\rangle f\right\}. \quad (5)$$

The two terms on the left-hand side are the time rate of change and the advection in physical space. The first three terms on the right-hand side are transport in velocity space of the JPDF by the SGS stress divergence, the resolvable-scale pressure gradient, and the buoyancy force, respectively. The last term is transport in scalar space by the SGS scalar flux divergence. The viscous force and scalar diffusion terms are small and are omitted at high Reynolds numbers.

Because SGS turbulence is usually studied by analyzing the SGS stress and flux rather than their divergences, an alternative form of the equation was given by Chen *et al.* (2005):

$$\begin{aligned}\frac{\partial f}{\partial t} + v_j \frac{\partial f}{\partial x_j} &= \frac{\partial^2}{\partial v_i \partial x_j}\left\{\langle \tau_{ij}|\mathbf{u^r} = \mathbf{v}, \theta^r = \psi \rangle f\right\} \\ &+ \frac{\partial^2}{\partial v_i \partial v_k}\left\{\left\langle -\frac{1}{2}P_{ij}|\mathbf{u^r} = \mathbf{v}, \theta^r = \psi \right\rangle f\right\} \\ &+ \frac{\partial^2}{\partial \psi \partial x_i}\left\{\langle F_i|\mathbf{u^r} = \mathbf{v}, \theta^r = \psi \rangle f\right\} \\ &+ \frac{\partial^2}{\partial \psi \partial v_k}\left\{\langle P_{Fi}|\mathbf{u^r} = \mathbf{v}, \theta^r = \psi \rangle f\right\} \\ &+ \frac{\partial^2}{\partial \psi \partial \psi}\left\{\langle P_\theta|\mathbf{u^r} = \mathbf{v}, \theta^r = \psi \rangle f\right\} \\ &+ \frac{\partial^2}{\partial v_i \partial x_i}\left\{\langle p^r|\mathbf{u^r} = \mathbf{v}, \theta^r = \psi \rangle f\right\} \\ &+ \frac{\partial^2}{\partial v_i \partial v_k}\left\{\left\langle p^r \frac{\partial u_k^r}{\partial x_i}|\mathbf{u^r} = \mathbf{v}, \theta^r = \psi \right\rangle f\right\} \\ &+ \frac{\partial^2}{\partial v_i \partial \psi}\left\{\left\langle p^r \frac{\partial \theta^r}{\partial x_i}|\mathbf{u^r} = \mathbf{v}, \theta^r = \psi \right\rangle f\right\} \\ &- \frac{g}{\Theta}\frac{\partial}{\partial v_3}\left\{\langle \theta^r|\mathbf{u^r} = \mathbf{v}, \theta^r = \psi \rangle f\right\}, \end{aligned} \quad (6)$$

where $P_{ij} = -\left\{\tau_{ik}\frac{\partial u_j^r}{\partial x_k} + \tau_{jk}\frac{\partial u_i^r}{\partial x_k}\right\}, P_{Fi} = -\left\{\tau_{ik}\frac{\partial \theta^r}{\partial x_k} + F_k \frac{\partial u_i^r}{\partial x_k}\right\}$, and $P_\theta = -F_i\frac{\partial \theta^r}{\partial x_i}$ are the SGS stress production rate, the SGS scalar flux production rate, and the SGS scalar variance production rate, respectively. The terms on the right-hand side now are mixed transport in velocity, physical, and scalar spaces due to the SGS stress, the SGS stress production rate, the SGS scalar flux, the SGS scalar flux production rate, the SGS scalar variance production rate, the resolvable-scale pressure, the pressure-strain correlation, the pressure-scalar-gradient correlation, and the buoyancy force, respectively. Therefore, the necessary conditions for LES to correctly predict the resolvable-scale velocity-scalar JPDF are that the conditional SGS stress, the conditional SGS scalar flux, the conditional SGS stress production rate, the conditional SGS scalar flux production rate, the conditional SGS scalar variance production rate are reproduced by the SGS models (Chen *et al.* (2005)).

These conditions were used to study the dependences of the resolvable-scale velocity-scalar JPDF on the SGS turbulence in a turbulent jet (Chen *et al.* (2005)). The results show that the conditional SGS scalar flux and the conditional SGS scalar flux production rate have a strong dependence on the resolvable-scale velocity and scalar, indicating strong flow history effects. Chen and Tong (2006) investigated the SGS velocity field in the surface layer of the ABL and showed that the behaviors of the conditional SGS stress and the conditional SGS stress production rate are closely related to the surface dynamics, i.e., updrafts generated by buoyancy force, downdrafts associated with the large-scale convective eddies, the mean shear, and the length scale inhomogeneity in the vertical direction. In addition, they found that the conditional SGS stress and the conditional SGS stress production rate have similar trends, and their eigenvectors are generally well aligned with the normalized tensorial contraction being close to one, thereby indicating the potential of modeling the conditional SGS stress using its production rate.

In present work we investigate the effects of the SGS motions on the resolvable-scale velocity-scalar JPDF in unstable atmospheric surface layer using measurement data. The field program and the array filter technique for measuring resolvable- and subgrid- scale variables are given in section 2. Section 3 examines the measured conditional SGS statistics and the SGS model predictions. The conclusions are given in section 4.

2. HATS FIELD PROGRAM

The field measurements for this study, named the horizontal array turbulence study, or HATS field program, were conducted at a field site 5.6km East-Northeast of Kettleman City, California, in the summer of 2000 as a collaboration primarily among the National Center for Atmospheric Research, Johns Hopkins University, and Penn State University (CT was part of the Penn State group). Horst *et al.* (2004) describe the field site and the data collection procedures in detail.

The field measurement design is based on the transverse array technique proposed, studied, and first used by the Penn State group (Edsall *et al.* (1995); Tong *et al.* (1997, 1998, 1999)) for surface layer measurements in the ABL. It has subsequently been used by several groups in the ABL over land (Tong *et al.* (1997, 1999); Porté-Agel *et al.* (2001); Kleissl *et al.* (2003); Horst *et al.* (2004)) and ocean (the recent ocean HATS program) as well as in engineering flows (Cerutti *et al.* (2000); Tong (2001); Wang and Tong (2002); Rajagopalan and Tong (2003); Chen *et al.* (2003); Wang *et al.* (2004)). The technique uses horizontal sensor arrays (figure 1) to perform two-dimensional filtering to obtain resolvable- and subgrid-scale variables. Two arrays are vertically spaced to obtain vertical derivatives. The primary horizontal array consists of nine equally spaced sonic anemometers (Campbell Scientific (SAT3)) and the secondary array has five sonics at a second height. The arrays are aligned perpendicular to the prevailing wind direction.

The filter operation in the streamwise direction is performed by invoking Taylor's hypothesis. Filtering in the transverse direction is realized by averaging the output of the signals from the sensor array (Tong *et al.* (1998)). For example, the transversely filtered resolvable-scale velocity (denoted by a superscript t) is obtained as

$$u_i^t(\mathbf{x},t) = \sum_{j=-N}^{N} C_j u_i(x_1, x_2 + j \times d, x_3, t) \qquad (7)$$

where $2N+1, C_j$, and d are the number of sensors on a array, the weighting coefficient for the jth sensor, and the spacing between adjacent sensors, respectively. We use $2N+1=5$ and 3 for filtering at the heights of the primary and secondary arrays respectively, to maintain the same filter size. The subgrid-scale velocity is obtained by subtracting the resolvable-scale part from the

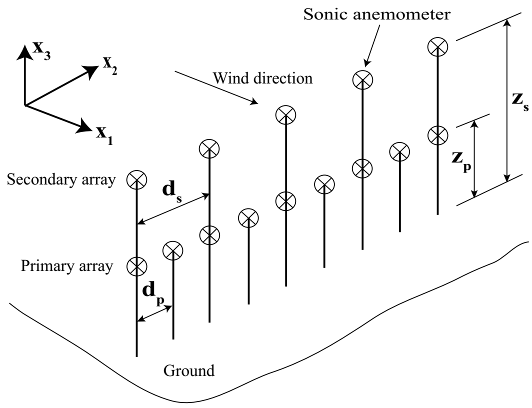

Figure 1: Schematic of the array setup. The secondary array (denoted by a subscript s) is used to obtain derivatives in the vertical direction.

total velocity. In the present study we use the arrays to approximate top-hat filters, which are the most compact type in physical space. Because derivatives are computed using finite differencing (with a spacing of $4d_p$ in the horizontal directions), which is effectively a top-hat filter, top-hat filters provide consistency among the resolvable-scale velocity and its derivatives.

The issues in applying the array filtering technique, including the accuracy of the array filter and the use of Taylor's hypothesis, have been systematically studied by Tong *et al.* (1998). They showed that a two-dimensional filter is a good approximation of a three-dimensional filter. They demonstrated that among the mechanisms that could affect the accuracy of Taylor's hypothesis (Lumley (1965)), including the effect of different convection velocity for different wavenumber components, temporal changes in the reference moving with the mean velocity, and the fluctuating convecting velocity, only the last one is significant. Their analyses of the accuracy of a spectral cutoff array filter as an approximation of true two-dimensional filter showed that the rms values of the filtered variables differ by less than 10%. Because the spectral cutoff filter has the slowest decay in physical space, it is most difficult to approximate by the array. Therefore, the accuracy of the top-hat filter array filter is expected to be higher. The error associated with one-side finite differencing in the vertical direction is examined by Kleissl *et al.* (2003). They evaluated the divergence-free condition for the filter velocity field and concluded that reasonable accuracy can be achieved in computing derivatives of filtered velocity. Horst *et al.* (2004) further studied various issues of using the array technique including the aliasing errors associated with evaluating derivatives using finite diffferencing and also demonstrated sufficient accuracy of the technique.

Four different array configurations, shown in Table 1, are employed in the HATS program. The filter (grid) aspect ration (Δ/z) ranges from 0.48 to 3.88, allowing the effects of grid anisotropy to be examined. We refer to z as the height of the primary array z_p here and there-

Array #	Δ/z_p	z_p	d_p	z_s	d_s
1	3.88	3.45	3.35	6.90	6.70
2	2.00	4.33	2.167	8.66	4.33
3	1.00	8.66	2.167	4.33	1.08
4	0.48	4.15	0.50	5.15	0.625

Table 1: Configurations of the four arrays (lengths in meters).

after. Array 3 is at a much higher z, therefore the effects of the stability parameter $-z/L$ can be examined, where $L = -\frac{u_*^3\Theta}{k_a g\langle u_3'\theta'\rangle}$, $u_*^2 = -\langle u_1'u_3'\rangle$ (a prime denotes fluctuations), $k_a = 0.41$, and g are the Monin-Obukov length, friction velocity, von Kármán constant, and gravitational acceleration, respectively. The surface layer parameters for the data sets collected using the four arrays are given in tables 2 and 3. The results in section 3.3 show that the SGS stress for array 1 which has the largest Δ/z, is the most anisotropic and most difficult for SGS models to predict, therefore our discussions of results focus on array 1. All array 1 data used in the present study were collected during daytime under clear conditions and the boundary layer was convective with a Monin-Obukov length of approximately -15m.

Although the arrays were arranged to be perpendicular to the prevailing wind direction, the mean wind direction for a given data section might not be exactly perpendicular to the array. Therefore, we rotate the coordinate system and interpolate the velocity and temperature in the Cartesian coordinate system defined by mean wind and cross-wind directions (Horst *et al.* (2004)). The interpolation is performed in spectral space to avoid attenuating the high frequency (wavenumber) fluctuations.

In present work, we study the unstable surface layer, i.e. $z/L < 0$. Data sections that are quasi-stationary are generally 30-90 minutes in length. In order to achieve reasonable statistical convergence in our analysis, we need to combine the results of selected data sections collected under similar stability conditions using the each array configuration. We focus on four data sections collected using array 1 (table 2). The conditional statistics obtained using the individual data sets (not shown) are very similar but with varying degree of uncertainty. Therefore, we normalize the results for each data set using its parameters, then weight-average them according to the number of conditional samples in each bin.

Due to the complexity of the variables of interest and of the conditional sampling procedure, we are not able to provide a precise level of statistical uncertainty. However, by monitoring the statistical scatter while increasing the data size, we conclude that reasonable statistical convergence is achieved. An example of the convergence process is given in Chen and Tong (2006). In addition, comparisons between model predictions and measurements only require the relative magnitude of the results and are less affected by the uncertainty. Therefore, the data size is sufficient for obtaining reliable statistics for the analyses.

3. RESULTS

In this section we focus our discussions on results obtained using data from array 1. The stability parameter $-z/L$ has an average value of 0.24. Top-hat filters in both the streamwise and crossstream directions are used to obtain the resolvable-scale and subgrid-scale variables with a filter size $\Delta = 3.88z$, which is in the energy-containing range. The results for the other array configurations, i.e. different Δ/z, and $-z/L$ (table 3), are also obtained. The results are generally similar to those for array 1 and will not be discussed. Table 4 gives the normalized Reynolds scalar flux and the ratios of the mean SGS scalar flux components to the vertical mean scalar flux. Array 1 has the largest fraction of the vertical SGS scalar flux and thus is the most challenging case for modeling. The measured and modeled SGS scalar flux components are given in table 5 and discussed in section 3.3.

The results for the conditional SGS stress $\langle\tau_{ij}|\mathbf{u}^r,\theta^r\rangle$ are normalized by the friction velocity u_*^2. The conditional SGS stress production rate $\langle P_{ij}|\mathbf{u}^{\mathbf{r}},\theta^r\rangle$ is normalized by the estimated energy dissipation rate $\epsilon = \theta_\epsilon\frac{u_*^3}{k_a z}$, where $\theta_\epsilon = 1 - z/L$ for $z/L \le 0$ as suggested by Kaimal *et al.* (1972). The conditional SGS scalar flux $\langle F_i|\mathbf{u}^{\mathbf{r}},\theta^r\rangle$ is normalized by the mean vertical heat flux $H = \langle\theta' u_3'\rangle$, where prime denotes fluctuations. The conditional SGS scalar flux production rate $\langle P_{Fi}|\mathbf{u}^{\mathbf{r}},\theta^r\rangle$ is normalized by $\frac{-T_* u_*^2}{z}$ where $T_* = -\frac{H}{u_*}$ is the temperature scale. The results for the conditional SGS variance spectral transfer rate $\langle P_\theta|\mathbf{u}^{\mathbf{r}},\theta^r\rangle$ are normalized by the estimated scalar variance transfer rate $\chi_T = \theta_h\frac{T_*^2 u_*}{k_a z}$, where $\theta_h = 0.74\times(1-9z/L)^{-1/2}$ for $z/L \le 0$ as suggested by Businger *et al.* (1971).

3.1. *SGS scalar flux and its production rate*

The results for the conditional SGS scalar flux components $\langle F_1|\mathbf{u}^r,\theta^r\rangle$, $\langle F_2|\mathbf{u}^r,\theta^r\rangle$, and $\langle F_3|\mathbf{u}^r,\theta^r\rangle$ are shown in figure 2. For convenience we omit the sample-space variable $\mathbf{v}$ and ψ from the conditional means here and hereafter. In addition, only the fluctuation parts of $\mathbf{u}^r$ and θ, which normalized by their respective r.m.s. values, are plotted.

The results show that $\langle F_1|\mathbf{u}^r,\theta^r\rangle$ and $\langle F_3|\mathbf{u}^r,\theta^r\rangle$ depend strongly on u_1^r and u_3^r for positive and small θ^r fluctuations, and the dependence is weak for negative θ^r fluctuations. $\langle F_2|\mathbf{u}^r,\theta^r\rangle$ also depends on $|u_2^r|$ and u_3^r for positive and small θ^r fluctuations, and the dependence is weak for negative θ^r fluctuations. $\langle F_1|\mathbf{u}^r,\theta^r\rangle$ generally has large values, because the large temperature fluctuations are highly correlated with the streak structure in the surface layer.

The trends of the SGS scalar production rates $\langle P_{F1}|\mathbf{u}^r,\theta^r\rangle$, $\langle P_{F2}|\mathbf{u}^r,\theta^r\rangle$ and $\langle P_{F3}|\mathbf{u}^r,\theta^r\rangle$ (figure 3) are generally similar to those of $\langle F_1|\mathbf{u}^r,\theta^r\rangle$, $\langle F_2|\mathbf{u}^r,\theta^r\rangle$, and $\langle F_3|\mathbf{u}^r,\theta^r\rangle$, respectively, for positive and small θ^r

Data#	$\langle u \rangle$ (ms^{-1})	$-z/L$	u_* (ms^{-1})	ϵ (m^{2}s^{-3})	H (K · ms^{-1})	χ_T (K^{2}s^{-1})	Duration (min)
a	1.42	0.34	0.15	0.003	0.02	0.001	35
b	3.56	0.22	0.33	0.031	0.17	0.026	30
c	3.65	0.21	0.36	0.039	0.20	0.035	83
d	3.25	0.24	0.36	0.041	0.24	0.048	33

Table 2: Surface layer parameters for array 1 ($\Delta/z = 3.88$) under unstable conditions. The primary array height z_p is used for z.

Array	Δ/z ($\approx$)	$\langle u \rangle$ (ms^{-1})	$-z/L$	u_* (ms^{-1})	ϵ (m^{2}s^{-3})	H (K m s^{-1})	χ_T (K^{2}s^{-1})	Total duration (min)
2	2.00	3.09	0.36	0.30	0.020	0.15	0.017	257
3	1.00	4.22	0.60	0.34	0.018	0.19	0.009	591
4	0.48	2.73	0.35	0.30	0.021	0.15	0.017	60

Table 3: Surface layer parameters for the other arrays under unstable conditions. The primary array height z_p is used for z.

fluctuations, indicating the dominant influence of SGS scalar flux production rate on the evolution of SGS scalar flux, and the conditional equilibrium between production rate and the pressure destruction. The dependence on the resolvable-scale velocity for negative θ^r fluctuations is weak.

To better understand the connections between the conditional SGS scalar flux and its production rate, we expand $\langle P_{F1}|\mathbf{u}^r,\theta^r\rangle$ as

$$\langle P_{F1}|\mathbf{u}^r,\theta^r\rangle = -\left\langle F_1\frac{\partial u_1^r}{\partial x_1} + F_2\frac{\partial u_1^r}{\partial x_2} + F_3\frac{\partial u_1^r}{\partial x_3} + \tau_{11}\frac{\partial \theta^r}{\partial x_1} + \tau_{12}\frac{\partial \theta^r}{\partial x_2} + \tau_{13}\frac{\partial \theta^r}{\partial x_3}|\mathbf{u}^r,\theta^r\right\rangle. \quad (8)$$

The first three terms on the right hand side of Eq. 8 are the production rate due to the interactions between the SGS scalar flux components and the resolvable-scale velocity gradient components and the last three terms are the production due to the interactions between SGS stress and the resolvable-scale scalar gradient. Our results obtained from the data show that the leading components in $\langle P_{F1}|\mathbf{u}^r,\theta^r\rangle$ are $\left\langle -F_3\frac{\partial u_1^r}{\partial x_3}|\mathbf{u}^r,\theta^r\right\rangle$ and $\left\langle -\tau_{33}\frac{\partial \theta^r}{\partial x_3}|\mathbf{u}^r,\theta^r\right\rangle$, which have similar trends and magnitudes. The rest of terms are relatively small because the horizontal derivatives of u_1^r and θ^r are relatively small compared to their vertical derivatives. Therefore, we focus our discussion in the following on $-\left\langle F_3\frac{\partial u_1^r}{\partial x_3} + \tau_{13}\frac{\partial \theta^r}{\partial x_3}|\mathbf{u}^r,\theta^r\right\rangle$. Similarly, $\langle P_{F3}|\mathbf{u}^r,\theta^r\rangle$ can be expanded as:

$$\langle P_{F3}|\mathbf{u}^r,\theta^r\rangle = -\left\langle F_1\frac{\partial u_3^r}{\partial x_1} + F_2\frac{\partial u_3^r}{\partial x_2} + F_3\frac{\partial u_3^r}{\partial x_3} + \tau_{31}\frac{\partial \theta^r}{\partial x_1} + \tau_{32}\frac{\partial \theta^r}{\partial x_2} + \tau_{33}\frac{\partial \theta^r}{\partial x_3}|\mathbf{u}^r,\theta^r\right\rangle \quad (9)$$

The terms on the right-hand side of Eq. 9 are similar to those in Eq. 8. The dominant component in $\langle P_{F3}|\mathbf{u}^r,\theta^r\rangle$ is $\left\langle -\tau_{33}\frac{\partial \theta^r}{\partial x_3}|\mathbf{u}^r,\theta^r\right\rangle$. This is because the derivatives of u_3^r and θ^r in the horizontal directions are relatively small. Therefore, we focus our attention on $\left\langle -\tau_{33}\frac{\partial \theta^r}{\partial x_3}|\mathbf{u}^r,\theta^r\right\rangle$.

We now discuss the results for $\langle P_{F1}|\mathbf{u}^r,\theta^r\rangle$ and $\langle P_{F3}|\mathbf{u}^r,\theta^r\rangle$. For positive θ^r fluctuations, the eddies associated with updrafts generally come from the region near the ground, and contain large magnitudes of the vertical SGS flux and the SGS stress. They also likely to have experienced strong shear and vertical temperature gradient. Therefore, both F_3, τ_{33}, $\partial u_1^r/\partial x_3$ have large positive values while τ_{13} and $\partial\theta^r/\partial x_3$ have large negative values, resulting in negative $\left\langle -F_3\frac{\partial u_1^r}{\partial x_3}|\mathbf{u}^r,\theta^r\right\rangle$ and $\left\langle -\tau_{13}\frac{\partial \theta^r}{\partial x_3}|\mathbf{u}^r,\theta^r\right\rangle$, and positive $\left\langle -\tau_{33}\frac{\partial \theta^r}{\partial x_3}|\mathbf{u}^r,\theta^r\right\rangle$. Because both the vertical shear, flux, and temperature gradient are enhanced by positive values of u_1^r and u_3^r, the magnitudes of $\langle P_{F1}|\mathbf{u}^r,\theta^r\rangle$ and $\langle P_{F3}|\mathbf{u}^r,\theta^r\rangle$ increase with u_1^r and u_3^r.

For small θ^r fluctuations, the eddies are generally well mixed, and therefore, tend to be more symmetric in the vertical direction, which is reflected by the symmetry of $\partial u_1^r/\partial x_3$ and $\partial\theta^r/\partial x_3$ respective to u_3^r. Therefore, the magnitudes of $\langle P_{F1}|\mathbf{u}^r,\theta^r\rangle$ and $\langle P_{F3}|\mathbf{u}^r,\theta^r\rangle$ increase with u_1^r and $|u_3^r|$.

For negative θ^r fluctuations, the eddies associated with downdrafts generally come from the mixed layer region, and contain relatively small SGS fluxes (figure 2(c)). Therefore, the magnitudes of $\langle P_{F1}|\mathbf{u}^r,\theta^r\rangle$ and $\langle P_{F3}|\mathbf{u}^r,\theta^r\rangle$ are small and have weak dependences on the resolvable-scale velocity.

Comparing the three cases of different θ^r values, the location of peak values of the conditional SGS scalar flux production rate appears to shift toward positive u_3^r for positive θ^r fluctuations, and toward negative u_3^r for negative θ^r fluctuations. This is because $\langle\partial u_1^r/\partial x_3|\mathbf{u}^r,\theta^r\rangle$ and $\langle\partial\theta^r/\partial x_3|\mathbf{u}^r,\theta^r\rangle$ (not shown) have similar trends, which indicates that the local gradients are enhanced by

Array	$\langle u_1'\theta'\rangle/H$	$\langle u_2'\theta'\rangle/H$	$\langle F_1\rangle/H$	$\langle F_2\rangle/H$	$\langle F_3\rangle/H$
1	-1.70	-0.23	-0.96	-0.00	0.70
2	-1.20	0.04	-0.62	0.02	0.56
3	-0.85	0.35	-0.26	0.01	0.33
4	-1.16	-0.21	-0.10	0.01	0.18

Table 4: Measured Reynolds scalar flux and mean SGS scalar flux for the four arrays

both updrafts with high temperature (positive θ^r fluctuations) and downdrafts with low temperature (negative θ^r fluctuations).

The conditional SGS scalar flux and the conditional SGS scalar flux production rate have similar trends for positive θ^r fluctuations, which is consistent with the balance between the production rate and pressure destruction and the use of the SGS scalar flux and a time scale to model the pressure destruction. The differences between the trends of the conditional SGS scalar flux and the conditional SGS scalar flux production rate for small and negative θ fluctuations are probably because the production rates are small and no longer balance the pressure destruction.

The dominant components in $\langle P_{F1}|\mathbf{u}^r,\theta^r\rangle$ contains a slow term $\left\langle -F_3\frac{\partial u_1^r}{\partial x_3}|\mathbf{u}^r,\theta^r\right\rangle$, in which F_3 influences $\langle P_{F1}|\mathbf{u}^r,\theta^r\rangle$ through the interaction with $\partial u_1^r/\partial x_3$. However F_1 does not have a direct effect on $\langle P_{F3}|\mathbf{u}^r,\theta^r\rangle$, which is dominated by $\left\langle \tau_{33}\frac{\partial\theta^r}{\partial x_3}|\mathbf{u}^r,\theta^r\right\rangle$. Consequently, accurate modeling of the vertical SGS scalar flux component may be more important than that of the horizontal SGS scalar flux component and poor predictions of the vertical SGS scalar flux component by a SGS model may result in the inaccuracies in the horizontal SGS scalar flux in a LES. In addition, because $\left\langle -\tau_{13}\frac{\partial\theta^r}{\partial x_3}|\mathbf{u}^r,\theta^r\right\rangle$ affects $\langle P_{F1}|\mathbf{u}^r,\theta^r\rangle$ due to the dominant vertical derivative of resolvable-scale scalar, underpredictions of the condition SGS shear stress components by a SGS model may also result in the inaccuracies in the conditional horizontal SGS scalar flux in a LES.

3.2. *SGS scalar variance production rate*

The SGS scalar variance production rate $\langle P_\theta|\mathbf{u}^r,\theta^r\rangle$ (figure 4) generally increase with u_1^r and u_3^r and the dependence is strong for positive θ^r fluctuations and weak for negative θ^r fluctuations. For small θ^r fluctuations, the dependence of $\langle P_\theta|\mathbf{u}^r,\theta^r\rangle$ on u_3^r is symmetric and increases with $|u_3^r|$. Similar to the SGS scalar flux production rate, the dominant component of $\langle P_\theta|\mathbf{u}^r,\theta^r\rangle$ is $\left\langle F_3\frac{\partial\theta^r}{x_3}|\mathbf{u}^r,\theta^r\right\rangle$. Because both F_3 and $\partial\theta^r/\partial x_3$ increase with u_1^r and u_3^r for positive θ^r, so does $\langle P_\theta|\mathbf{u}^r,\theta^r\rangle$. The symmetric dependence of $\langle P_\theta|\mathbf{u}^r,\theta^r\rangle$ on u_3^r is due to the symmetric dependence of $\partial\theta^r/\partial x_3$ on u_3^r.

3.3. *Alignment of SGS scalar flux and its production rate*

Chen and Tong (2006) found that the deviatoric part of $\langle\tau_{ij}|\mathbf{u^r}\rangle$ and $\langle P_{ij}|\mathbf{u^r}\rangle$ have similar trends, and the eigenvectors of $\langle\tau_{ij}|\mathbf{u^r}\rangle$ and $\langle P_{ij}|\mathbf{u^r}\rangle$ are well aligned with the normalized tensorial contraction being close to unity, indicating the balance between the production rate and pressure destruction and the validity of using the SGS stress and a time scale for modeling the pressure destruction. The results in part 1 also show that $\langle F_i|\mathbf{u}^r,\theta^r\rangle$ and $\langle P_{Fi}|\mathbf{u}^r,\theta^r\rangle$ have similar trends. To investigate the relationship between $\langle F_i|\mathbf{u}^r,\theta^r\rangle$ and $\langle P_{Fi}|\mathbf{u}^r,\theta^r\rangle$, we compute the alignment angle between $\langle F_i|\mathbf{u}^r,\theta^r\rangle$ and $\langle P_{Fi}|\mathbf{u}^r,\theta^r\rangle$, which is given by

$$\alpha = \cos^{-1}\left(\frac{|\langle F_i|\mathbf{u}^r,\theta^r\rangle\cdot\langle P_{Fi}|\mathbf{u}^r,\theta^r\rangle|}{\|\langle F_i|\mathbf{u}^r,\theta^r\rangle\|\cdot\|\langle P_{Fi}|\mathbf{u}^r,\theta^r\rangle\|}\right) \quad (10)$$

Figure 5 shows that $\langle F_i|\mathbf{u}^r,\theta^r\rangle$ and $\langle P_{Fi}|\mathbf{u}^r,\theta^r\rangle$ are generally well aligned. The alignment angle α is generally less than 10° for positive and small θ^r fluctuations. For negative θ^r fluctuations, the alignment angle is small for positive u_3^r and larger (less than 30°) for negative u_3^r. This is probably due to the small magnitudes of $\langle P_{Fi}|\mathbf{u}^r,\theta^r\rangle$, suggesting imbalance between production and destruction.

In order to study the effects of buoyancy on the alignment, the buoyancy production term ($P_{FB} = \frac{g}{\Theta}[(\theta^2)^r - (\theta^r)^2]$) is included in the SGS scalar flux production rate. The alignment angle (figure 5(b)) increase slightly, indicating that buoyancy does not significantly alter the alignment property.

These results are consistent with the similarity between the conditional SGS scalar flux and the conditional SGS scalar flux production rate, suggesting the balance between the production rate and pressure destruction and the validity of using the SGS scalar flux and a time scale for modeling the pressure destruction.

3.4. *SGS stress and its production rate*

The normalized conditional SGS stress components $\langle\tau_{11}|\mathbf{u}^r,\theta^r\rangle$ and $\langle\tau_{33}|\mathbf{u}^r,\theta^r\rangle$ are given in figure 6. The results show that $\langle\tau_{11}|\mathbf{u}^r,\theta^r\rangle$ and $\langle\tau_{33}|\mathbf{u}^r,\theta^r\rangle$ generally increase with u_1^r and u_3^r. The dependences are strong for positive θ^r fluctuations and are weak for negative θ^r fluctuations.

The conditional SGS stress production rate $\langle P_{11}|\mathbf{u}^r,\theta^r\rangle$ (figure 7 (a)) has a similar trend to $\langle\tau_{11}|\mathbf{u}^r,\theta^r\rangle$ (figure 6(a)), suggesting that there is a local conditional equilibrium between the SGS stress production rate and the pressure destruction. However, the trend of $\langle P_{33}|\mathbf{u}^r,\theta^r\rangle$ (figure 7(b)) is different from $\langle \tau_{33}|\mathbf{u}^r,\theta^r\rangle$ (figure 6(b)) because the buoyancy production rate dominates the evolution of $\langle \tau_{33}|\mathbf{u}^r,\theta^r\rangle$, consistent with our previous results (Chen *et al.* (2005)).

The dependence of $\langle P_{33}|\mathbf{u}^r,\theta^r\rangle$ decreases with θ^r fluctuations. For positive θ^r fluctuations, conditional $\langle P_{11}|\mathbf{u}^r,\theta^r\rangle$ has positive values, indicating τ_{11} gains energy while $\langle P_{33}|\mathbf{u}^r,\theta^r\rangle$ has negative values, indicating that τ_{33} loses energy and conditional backscatter. For negative θ^r fluctuations, $\langle P_{33}|\mathbf{u}^r,\theta^r\rangle$ is positive, indicating that τ_{33} gains energy. Our previous study (Chen and Tong (2006)) has shown that underprediction of the dependence of $\langle P_{33}|\mathbf{u}^r,\theta^r\rangle$ on u_3^r will cause the same for the vertical velocity skewness. This will be further examined along with SGS models in section 3.7.

The conditional shear stress component $\langle \tau_{13}|\mathbf{u}^r,\theta^r\rangle$ (figure 8(a)) depends on u_1^r and u_3^r, and the dependence is strong for positive θ^r fluctuations and weak for negative θ^r fluctuations. $\langle P_{13}|\mathbf{u}^r,\theta^r\rangle$ (figure 8(b)) has a similar trend, indicating the conditional quasi-equilibrium.

Our previous study (Chen and Tong (2006)) has shown that underpredictions of the trend and magnitude of the τ_{13} cause overpredictions of the mean streamwise velocity gradient near the surface, and that the correct prediction of $\langle \tau_{13}|\mathbf{u}^r\rangle$ is very important for predicting the horizontal velocity variance profile.

The dependence of $\langle \tau_{ij}|\mathbf{u}^r,\theta^r\rangle$ on θ^r is partly due to the flow history effect. A velocity field is not affected by a passive scalar. The dependence of the conditional SGS stress and conditional SGS stress production rate on the resolvable-scale scalar reflects the different flow histories that the SGS eddies with the same resolvable-scale velocity but different resolvable-scale scalar values have experienced (Chen *et al.* (2005)). The temperature in the ABL is generally not passive, therefore, the dependence is probably partly due to the flow history and partly due to the buoyancy effects. The dependence on u^r for positive temperature fluctuations is very close to the dependence on u^r alone. This is because the buoyancy force and thermal plumes are associated with positive temperature fluctuations. For negative temperature fluctuations, the dependence is generally weak.

3.5. *Anisotropy of the conditional SGS stress*

An important property of the SGS stress is its level of anisotropy. The level of anisotropy of the conditional SGS stress can be characterized by the representation in the Lumley triangle (Lumley (1978)). The normalized anisotropy tensor for $\langle \tau_{ij}|\mathbf{u}^r,\theta^r\rangle$, $\frac{\langle \tau_{ij}|\mathbf{u}^r,\theta^r\rangle}{\langle \tau_{kk}|\mathbf{u}^r,\theta^r\rangle}-\frac{1}{3}\delta_{ij}$, can be determined by two variables ξ and η defined in terms of its invariants (Pope (2000))

$$6\eta^2=-2II=\frac{\left\langle \tau^d_{ij}|\mathbf{u}^r,\theta^r\right\rangle\left\langle \tau^d_{ij}|\mathbf{u}^r,\theta^r\right\rangle}{\langle \tau_{kk}|\mathbf{u}^r,\theta^r\rangle^2} \tag{11}$$

and

$$6\xi^3=3III=\frac{\left\langle \tau^d_{ij}|\mathbf{u}^r,\theta^r\right\rangle\left\langle \tau^d_{jk}|\mathbf{u}^r,\theta^r\right\rangle\left\langle \tau^d_{ki}|\mathbf{u}^r,\theta^r\right\rangle}{\langle \tau_{kk}|\mathbf{u}^r,\theta^r\rangle^3}, \tag{12}$$

where $\tau^d_{ij}=\tau_{ij}-\tau_{kk}\delta_{ij}/3$ is the deviatoric part of the SGS stress, and II and III are the second and third invariants of the anisotropy tensor respectively. If $\langle \tau_{ij}|\mathbf{u}^r,\theta^r\rangle$ is isotropic, both ξ and η are zero. (The first invariant or trace of $\left\langle \tau^d_{ij}|\mathbf{u}^r,\theta^r\right\rangle$ is always zero by definition). The representation for the conditional SGS stress results are shown in figure 9. The dependence of the anisotropy on the resolvable-scale velocity (Lumley triangle for $\langle \tau_{ij}|\mathbf{u}^r\rangle$) Chen and Tong (2006) shows that the anisotropy is weak for negative u_3^r and is much stronger for positive u_3^r. For positive and negative u_1^r values, $\langle \tau_{ij}|\mathbf{u}^r\rangle$ is close to axisymmetric with one large and one small eigenvalue, respectively, probably reflecting the shear and buoyancy effects. Here we study the dependence of the anisotropy on the resolvable-scale scalar.

Figure 9 shows that there is a clear dependence of the anisotropy on the resolvable-scale scalar. For positive and small θ^r fluctuations, $\langle \tau_{ij}|u_1^r,u_3^r,\theta^r\rangle$ is quite anisotropic and close to the results for $\langle \tau_{ij}|u_1^r,u_3^r\rangle$ (without conditioning on θ^r), consistent with the trends of $\langle \tau_{ij}|\mathbf{u}^r,\theta^r\rangle$ in section 3.2.1. The points representing the anisotropy are not far from $\eta=-\xi$ and $\eta=\xi$ indicating that $\langle \tau_{ij}|u_1^r,u_3^r,\theta^r\rangle$ is close to axisymmetric with either one small eigenvalue or one large eigenvalue. One difference between the results for small θ^r fluctuations and for positive θ^r fluctuations is that there are more points close to $\eta=\xi$ than that of $\eta=-\xi$, indicating that the SGS eddies are more likely to contain SGS stress that is close to axisymmetric with one large eigenvalue. This is probably because the compression and shear effects are weakened as these eddies are likely to has gone through a strong mixing process.

For negative θ^r fluctuations, there are more points representing the anisotropy close to the origin than for positive and small θ^r fluctuations, indicating a slightly less anisotropic SGS stress. In addition, some points with $u_3^r<0$ are close to the axisymmetric with one small eigenvalue ($\eta=-\xi$) due to the compression effect, and some points with $u_3^r>0$ are close to the axisymmetric with one large eigenvalue ($\eta=\xi$) due to the weakened shear effect.

3.6. *Alignment between the conditional SGS stress and its production rate*

The geometric alignment of $\left\langle \tau^d_{ij}|\mathbf{u}^r,\theta^r\right\rangle$ and $\left\langle P^a_{ij}|\mathbf{u}^r,\theta^r\right\rangle$ can be characterized by the angles between their eigenvectors. The alignment between $\left\langle \tau^d_{ij}|\mathbf{u}^r\right\rangle$ and $\left\langle P^a_{ij}|\mathbf{u}^r\right\rangle$ ($P^a_{ij}=P_{ij}-P_{kk}\delta_{ij}/3$) were first studied by Chen and Tong (2006). They found that $\left\langle \tau^d_{ij}|u_3^r\right\rangle$ and $\left\langle P^a_{ij}|u_3^r\right\rangle$ are well aligned for positive u_3^r with the alignment angles are less than 10° but are less well aligned for negative u_3^r.

We further examine the dependence of the alignment between the conditional SGS stress and its production rate on temperature fluctuations. The alignment angles are defined in the same way as those in Chen & Tong 2006 Chen and Tong (2006). The eigenvalues of the conditional SGS stress tensor, $\left\langle \tau^d_{ij}|\mathbf{u}^r,\theta^r\right\rangle$, are denoted as α_τ,β_τ and γ_τ, ordered such that $\alpha_\tau\geq\beta_\tau\geq\gamma_\tau$,

	$\langle F_1\rangle/H$	$\langle F_2\rangle/H$	$\langle F_3\rangle/H$
F_i^{smg}	-0.003	-0.003	0.51
F_i^{nl}	-1.31	0.03	0.13
F_i^{mix}	-1.31	0.03	0.54

Table 5: Modeled mean SGS scalar flux for array 1

and the corresponding unit eigenvectors as $\vec{\alpha}_\tau, \vec{\beta}_\tau$ and $\vec{\gamma}_\tau$. Similarly, the eigenvalues of the conditional SGS stress production tensor, $\left\langle P_{ij}^a|\mathbf{u}^r, \theta^r\right\rangle$, are denoted as α_P, β_P and γ_P, ordered such that $\alpha_P \geq \beta_P \geq \gamma_P$, and the corresponding unit eigenvectors as $\vec{\alpha}_P, \vec{\beta}_P$ and $\vec{\gamma}_P$. Three alignment angles, ψ, ϕ and ξ, are defined as $\psi = \cos^{-1}(|\vec{\gamma}_P \cdot \vec{\gamma}_\tau|)$ (the angle between $\vec{\gamma}_P$ and $\vec{\gamma}_\tau$), $\phi = \cos^{-1}(|\vec{\beta}_P \cdot \vec{\beta}_\tau|)$, and $\xi = \cos^{-1}(|\vec{\alpha}_P \cdot \vec{\alpha}_\tau|)$.

The results for the alignment angles are given in figure 10. The results show that $\left\langle \tau_{ij}^d|\mathbf{u}^r, \theta^r\right\rangle$ and $\left\langle P_{ij}^a|\mathbf{u}^r, \theta^r\right\rangle$ are generally well aligned for positive u_3^r and is less well aligned for negative u_3^r, and that the alignment angles weakly depend on u_1^r, which is similar to the results of Chen and Tong (2006). Alignment angles are smaller for positive θ^r fluctuations and larger for negative θ^r fluctuations.

The results for the Lumley triangle (figure 9) show that SGS stress is more anisotropic for $u_3^r > 0$, therefore, there is likely a strong trend to return to isotropy, and therefore the pressure destruction can be predicted well by τ_{ij}/τ. In addition, the updrafts with higher temperature ($\theta^r > 0$) generally experience stronger shear and temperature gradients near ground with large production rate and the pressure destruction and production are balanced. Therefore, the SGS stress and its production rate are well aligned.

For $u_3^r < 0$, The Lumley triangle shows that the SGS stress is less anisotropic. The misalignment (or poor alignment) for $\theta^r < 0$, and $u_3^r < 0$ suggests that the pressure destruction is larger than the SGS production.

3.7. *SGS scalar flux model*

The results discussed in the previous parts of this section provide a basis for studying the effects of SGS models on LES statistics. Here we examine the model predictions of $\langle F_i|\mathbf{u}^r, \theta^r\rangle, \langle P_{Fi}|\mathbf{u}^r, \theta^r\rangle$ and $\langle P_\theta|\mathbf{u}^r, \theta^r\rangle$ using the Smagorinsky model, the nonlinear model, and the mixed model, and compare them to the experimental results. The mean values of the measured and modeled mean SGS scalar flux components are given in table 5.

In order to compute the modeled SGS scalar flux production rate P_{Fi}, the modeled SGS stress is needed. In this work, the modeled SGS stress is computed using the same procedure given by Chen and Tong (2006). Our previous study (Chen and Tong (2006)) shows that the conditional mean of the normal components are severely underpredicted by the Smagorinsky model and slightly overpredicted by the nonlinear model. The trends of the shear components are generally well predicted by the Smagorinsky model and are poorly predicted by the nonlinear model. The magnitudes of the shear components are generally underpredicted by a factor of two using the Smagorinsky model. The mixed model can predict normal components well but not the shear component. These results are important for understanding the trends and magnitudes of the conditional mean of the SGS scalar flux production rate discussed in the following.

3.7.1. *The Smagorinsky model*

The Smagorinsky model is given by Smagorinsky (1963) and Lilly (1967).

$$F_i^{smg} = -Pr_T^{-1}(C_S\Delta)^2(2S_{mn}S_{mn})^{1/2}\frac{\partial\theta^r}{\partial x_i} \qquad (13)$$

where $C_s = 0.154$ is the Smagorinsky constant for a box filter and Pr_T is the SGS turbulent Prandtl number, and S_{ij} is the resolvable-scale velocity strain rate. In this work, we determine $Pr_T^{-1}C_s^2$ by matching the mean SGS scalar variance production rate.

Tables 4 and 5 show that the mean horizontal SGS scalar flux is severely underpredicted by the Smagorinsky model and the mean vertical SGS scalar flux is underpredicted by approximately 30 percent. The predicted conditional means using the Smagorinsky model are shown in figure 11 and 12. Figures 11(a) and 2(a) shows that the horizontal SGS scalar flux, $\langle F_1|\mathbf{u}^r, \theta^r\rangle$ is underpredicted, because it use only the horizontal scalar gradient $\partial\theta^r/\partial x_1$, which is very small. The sign of $\langle F_1|\mathbf{u}^r, \theta^r\rangle$ is not predicted correctly. As discussed in section 3.1 the conditional production of F_1 is dominated by $\left\langle F_3\frac{\partial u_1^r}{\partial x_3}|\mathbf{u}^r, \theta^r\right\rangle$ and $\left\langle \tau_{13}\frac{\partial\theta^r}{\partial x_3}|\mathbf{u}^r, \theta^r\right\rangle$. However, these gradients do not appear in the model. Therefore the model cannot account for the dominant production mechanisms and consequently cannot predict the flux correctly. The results demonstrate the importance of including the effects of the dominant vertical gradient in the modeling of $\langle F_1|\mathbf{u}^r, \theta^r\rangle$.

Figure 11(b) and 2(c) shows that the magnitude of the vertical SGS scalar flux $\langle F_3|\mathbf{u}^r, \theta^r\rangle$ is better predicted than that of $\langle F_1|\mathbf{u}^r, \theta^r\rangle$. The trends of $\langle F_3|\mathbf{u}^r, \theta^r\rangle$ are generally well predicted for positive θ^r fluctuations. The trends for small θ^r fluctuations are somewhat less well predicted. Because $\langle F_3^{smg}|\mathbf{u}^r, \theta^r\rangle$ uses the gradients $\partial\theta^r/\partial x_3$ which is in the dominant term in P_{F3}, it is generally much better predicted than $\langle F_1^{smg}|\mathbf{u}^r, \theta^r\rangle$

The trend of $\langle P_{F1}|\mathbf{u}^r, \theta^r\rangle$ is generally well predicted (figure 12(a)). $\langle P_{F1}^{smg}|\mathbf{u}^r, \theta^r\rangle$ ($= -\left\langle \tau_{1k}^{smg}\frac{\partial\theta^r}{\partial x_k} + F_k^{smg}\frac{\partial u_1^r}{\partial x_k}|\mathbf{u}^r, \theta^r\right\rangle$) is dominated by the term $-\left\langle F_3^{smg}\frac{\partial u_1^r}{\partial x_3} + \tau_{13}^{smg}\frac{\partial\theta^r}{\partial x_3}|\mathbf{u}^r, \theta^r\right\rangle$. Therefore, the well predicted trend of $\langle P_{F1}|\mathbf{u}^r, \theta^r\rangle$ is due to the well predicted τ_{13} and F_3. However, the magnitude is underpredicted approximately by a factor of two due to the underprediction of the magnitude of τ_{13} (Chen and Tong (2006)) and F_3.

The trend and magnitude of $\langle P_{F3}|\mathbf{u}^r, \theta^r\rangle$ in figure 12(b) are poorly predicted. As discussed in section 3.1 $\langle P_{F3}^{smg}|\mathbf{u}^r, \theta^r\rangle$ ($= -\left\langle \tau_{3k}^{smg}\frac{\partial\theta^r}{\partial x_k} + F_k^{smg}\frac{\partial u_3^r}{\partial x_k}|\mathbf{u}^r, \theta^r\right\rangle$)

is dominated by the term $\left\langle -\tau_{33}^{smg}\frac{\partial\theta^r}{\partial x_3}|\mathbf{u}^r,\theta^r\right\rangle$. Therefore, the poor prediction of $\langle P_{F3}|\mathbf{u}^r,\theta^r\rangle$ is due to the poor prediction of τ_{33} by Smagorinsky model (Chen and Tong (2006)).

The trend and magnitude of $\langle P_\theta|\mathbf{u}^r,\theta^r\rangle$ in figure 12(c) are generally well predicted. The dominant term of $\langle P_\theta^{smg}|\mathbf{u}^r,\theta^r\rangle$ is $\left\langle F_3^{smg}\frac{\partial\theta^r}{\partial x_3}|\mathbf{u}^r,\theta^r\right\rangle$, therefore, the well predicted trend (the magnitude is matched) is due to the well predicted trend of F_3.

The results for the SGS production rates show that when the conditional means of the SGS stress and/or flux components that appear in a SGS production rate are well predicted by a SGS model, the conditional mean of the SGS production rate is also well predicted. This suggests that the correlations between the conditional fluctuations of the SGS stress (flux) and the resolvable-scale gradients are of less importance. Consequently, it appears to be sufficient to focus on the conditional means.

3.7.2. *The nonlinear model*

The nonlinear model (Leonard (1974); Clark *et al.* (1979)) is the first order approximation of the similarity model Bardina *et al.* (1980) and is given by:

$$F_i^{nl} = \frac{1}{12}\Delta^2\frac{\partial\theta^r}{\partial x_k}\frac{\partial u_i^r}{\partial x_k}. \tag{14}$$

The predictions of the nonlinear model are shown in figure 13 and 14. In general, the nonlinear model predicts the overall trend and the magnitude better than the Smagorinsky model. The trend for small θ^r fluctuations is underpredicted but the magnitude is slightly overpredicted.

The mean horizontal SGS scalar flux is overpredicted by approximately 35 percent and the mean vertical SGS scalar flux is underpredicted by approximately 80 percent. The predicted magnitude of $\langle F_1|\mathbf{u}^r,\theta^r\rangle$ using the nonlinear model is better than that of the Smagorinsky model. The better prediction of $\langle F_1|\mathbf{u}^r,\theta^r\rangle$ can be understood as following: the nonlinear model component $F_1^{nl} = \frac{\partial\theta^r}{\partial x_k}\frac{\partial u_1^r}{\partial x_k}$ is dominated by the term $\frac{\partial\theta^r}{\partial x_3}\frac{\partial u_1^r}{\partial x_3}$, which can be rewritten in terms of the Smagorinsky model as

$$F_1^{nl} \sim \frac{\partial\theta^r}{\partial x_3}\frac{\partial u_1^r}{\partial x_3} \propto F_3^{smg}\frac{\partial u_1^r}{\partial x_3} + \tau_{13}^{smg}\frac{\partial\theta^r}{\partial x_3}. \tag{15}$$

The previous section shows that τ_{13} and F_3 are well predicted by the Smagorinsky model. Therefore, the term $F_3^{smg}\frac{\partial u_1^r}{\partial x_3} + \tau_{13}^{smg}\frac{\partial\theta^r}{\partial x_3}$ in equation (15) is effectively the Smagorinsky model prediction of $\langle P_{F1}|\mathbf{u}^r,\theta^r\rangle$. Figure 2a, 3a, and 5a have shown that the conditional SGS flux and the conditional flux production rate have similar trends, which is likely a result of the balance between the SGS flux production rate and the pressure destruction and the fact that the latter can be well predicted by the SGS flux and a SGS time scale. Therefore, $\langle F_1|\mathbf{u}^r,\theta^r\rangle$ is better predicted by the nonlinear model.

The trend of $\langle F_3|\mathbf{u}^r,\theta^r\rangle$ is underpredicted. Furthermore, $\left\langle F_3^{nl}|\mathbf{u}^r,\theta^r\right\rangle$ has some spurious negative values. The magnitudes for positive values are underpredicted. The dominant component of F_3^{nl} is $\frac{\partial\theta^r}{\partial x_3}\frac{\partial u_3^r}{\partial x_3}$, which can be rewritten as

$$F_3^{nl} \sim \frac{\partial\theta^r}{\partial x_3}\frac{\partial u_3^r}{\partial x_3} \propto \tau_{33}^{smg}\frac{\partial\theta^r}{\partial x_3}. \tag{16}$$

Because τ_{33} is poorly modeled by the Smagorinsky model, $\frac{\partial\theta^r}{\partial x_3}\frac{\partial u_3^r}{\partial x_3}$ is not a good model for the dominant term of P_{F3}. Therefore, $\langle F_3|\mathbf{u}^r,\theta^r\rangle$ is poorly modeled by the nonlinear model.

The above analysis of the nonlinear model using the Smagorinsky model and the surface layer dynamics provides a physical explanation of the performance of the nonlinear model. Here we also provide a similar analysis of the nonlinear SGS stress model. The normal component of the nonlinear model τ_{11}^{nl} can be rewritten as $\tau_{11}^{nl} \sim \frac{\partial u_1^r}{\partial x_1}\frac{\partial u_1^r}{\partial x_1} + \frac{\partial u_1^r}{\partial x_2}\frac{\partial u_1^r}{\partial x_2} + \frac{\partial u_1^r}{\partial x_3}\frac{\partial u_1^r}{\partial x_3} \propto \tau_{11}^{smg}\frac{\partial u_1^r}{\partial x_1} + \tau_{12}^{smg}\frac{\partial u_1^r}{\partial x_2} + \tau_{13}^{smg}\frac{\partial u_1^r}{\partial x_3}$. Because the trend of τ_{13} is well predicted by the Smagorinsky model, $\tau_{13}^{smg}\frac{\partial u_1^r}{\partial x_3}$ is a good model for the dominant term in P_{11}, therefore, τ_{11} is well predicted. Similarly, the dominant term in τ_{33}^{nl}, $\frac{\partial u_3^r}{\partial x_3}\frac{\partial u_3^r}{\partial x_3}$, can be written as $\tau_{33}^{smg}\frac{\partial u_3^r}{\partial x_3}$. Because τ_{33} is poorly predicted by the Smagorinsky model, so is τ_{33} by the nonlinear model. The understanding can also be use to analyze the production rate $\left\langle P_{ij}^{nl}|\mathbf{u}^r,\theta^r\right\rangle$.

The magnitude and the trend of $\left\langle P_{F1}^{nl}|\mathbf{u}^r,\theta^r\right\rangle$ for positive θ^r fluctuations are not well predicted (figure 14(a)). This is due to the poor predictions of F_3 and τ_{13}, which are in the dominant terms in $\langle P_{F1}|\mathbf{u}^r,\theta^r\rangle$ ($-\left\langle F_3\frac{\partial u_1^r}{\partial x_3} + \tau_{13}\frac{\partial\theta^r}{\partial x_3}|\mathbf{u}^r,\theta^r\right\rangle$).

The magnitude of $\left\langle P_{F3}^{nl}|\mathbf{u}^r,\theta^r\right\rangle$ (figure 14(b)) is underpredicted, while the trend for positive θ^r fluctuations is better predicted than that for small and negative θ^r fluctuations. This is due to the well predicted trend of τ_{33}, which is in the dominant term of $\langle P_{F3}|\mathbf{u}^r,\theta^r\rangle$ ($\left\langle -\tau_{33}\frac{\partial\theta^r}{\partial x_3}|\mathbf{u}^r,\theta^r\right\rangle$).

The magnitude of $\langle P_\theta|\mathbf{u}^r,\theta^r\rangle$ is well predicted, whereas the trend is not as well predicted as the Smagorinsky model. This is due to the poor prediction of F_3, which is in the dominant term of $\langle P_\theta|\mathbf{u}^r,\theta^r\rangle$ ($\left\langle F_3\frac{\partial\theta^r}{\partial x_3}|\mathbf{u}^r,\theta^r\right\rangle$).

3.7.3. *The mixed model*

The previous results show that the Smagorinsky model can predict $\langle F_3|\mathbf{u}^r,\theta^r\rangle$ but not $\langle F_1|\mathbf{u}^r,\theta^r\rangle$, and the nonlinear model can predict well $\langle F_1|\mathbf{u}^r,\theta^r\rangle$ but not $\langle F_3|\mathbf{u}^r,\theta^r\rangle$. Therefore, a mixed model combining these two models

$$F_i^{mix} = \frac{1}{12}\Delta^2\frac{\partial\theta^r}{\partial x_k}\frac{\partial u_i^r}{\partial x_k} - Pr_T^{-1}(C_S\Delta)^2(2S_{mn}S_{mn})^{1/2}\frac{\partial\theta^r}{\partial x_i} \tag{17}$$

can potentially provide improved predictions.

The mean horizontal SGS scalar flux is overpredicted by approximately 35 percent and the mean vertical SGS scalar flux is underpredicted by approximately 23 percent. The results of the conditional means for the mixed model are shown in figure 15 and 16. The predicted magnitude and trend of $\langle F_1|\mathbf{u}^r,\theta^r\rangle$ are close to, but not quite as good as the predictions using the nonlinear model due to the underpredicted magnitude of $\langle F_1|\mathbf{u}^r,\theta^r\rangle$ by the Smagorinsky model. The predicted trend of $\langle F_3|\mathbf{u}^r,\theta^r\rangle$ is somewhat in between the predictions by the Smagorinsky model and the nonlinear models, because the magnitude of $\left\langle F_3^{nl}|\mathbf{u}^r,\theta^r\right\rangle$ is comparable to that of $\langle F_3^{smg}|\mathbf{u}^r,\theta^r\rangle$.

The magnitude and trend of $\left\langle P_{F1}^{mix}|\mathbf{u}^r,\theta^r\right\rangle$ are close to the predictions of the nonlinear model with improved magnitude. This is because F_3^{mix} and τ_{13}^{mix} are better than F_3^{nl} and τ_{13}^{nl}, but not as good as F_3^{smg} and τ_{13}^{smg}. The magnitude of $\left\langle P_{F3}^{mix}|\mathbf{u}^r,\theta^r\right\rangle$ is close to the predictions of the nonlinear model, because the magnitude of $\langle P_{F3}^{smg}|\mathbf{u}^r,\theta^r\rangle$ is smaller than that of $\left\langle P_{F3}^{nl}|\mathbf{u}^r,\theta^r\right\rangle$. The trend of $\left\langle P_\theta^{mix}|\mathbf{u}^r,\theta^r\right\rangle$ is in between those of $\left\langle P_\theta^{nl}|\mathbf{u}^r,\theta^r\right\rangle$ and $\langle P_\theta^{smg}|\mathbf{u}^r,\theta^r\rangle$. Therefore, the prediction of $\langle P_\theta|\mathbf{u}^r,\theta^r\rangle$ using the mixed model is not as good as that of the Smagorinsky model but better than that of the nonlinear model. Therefore, the mixed model offers a compromise between the Smagorinsky model and the nonlinear model.

3.8. *Potential effects of SGS models on the resolvable-scale statistics*

The results discussed above show that the conditional horizontal scalar flux production rate is dominated by $\left\langle -F_3\frac{\partial u_1^r}{\partial x_3}|\mathbf{u}^r,\theta^r\right\rangle$ and $\left\langle -\tau_{13}\frac{\partial \theta^r}{\partial x_3}|\mathbf{u}^r,\theta^r\right\rangle$, and the conditional vertical scalar flux production rate is dominated by $\left\langle -\tau_{33}\frac{\partial \theta^r}{\partial x_3}|\mathbf{u}^r,\theta^r\right\rangle$. Therefore, correct predictions of F_3, τ_{13} and τ_{33} are very important for reproducing the resolvable-scale velocity-scalar JPDF.

The Smagorinsky model underpredicts the conditional horizontal SGS scalar flux but predicts well the trend of the conditional vertical SGS scalar flux. The underprediction of the conditional horizontal SGS scalar flux directly affects the scalar PDF, and therefore the velocity-scalar JPDF.

The Smagorinsky model also underpredicts the conditional τ_{33} (Chen and Tong (2006)). Because τ_{33} appears in the dominant term of the conditional vertical scalar flux production rate, the underprediction of the conditional τ_{33} causes underprediction of the conditional vertical scalar flux production rate, which in turn results in underprediction of the resolvable-scale vertical scalar flux (velocity-temperature correlation). For a constant heat flux boundary condition, the mean scalar gradient will be overpredicted because the LES fields have to adjust themselves to carry the improved heat flux at the boundary. The improved mean scalar profile using the split model (Mason and Thomson (1992)) and stochastic model (Sullivan *et al.* (1994)) may be partly because these models have improved τ_{13} and τ_{33}, which is important for scalar flux production rate. Introducing backscatter can improved the scalar PDF as well and results in better scalar variance profile.

The nonlinear model can predict the conditional horizontal SGS scalar flux well but not the vertical SGS flux. Again due to the constant heat flux boundary condition the underprediction of the vertical SGS scalar flux causes overprediction of the mean scalar gradient. The underprediction of the conditional F_3 and τ_{13} also cause underprediction of the conditional P_{F1}, which results in underprediction of the horizontal resolvable-scale scalar flux.

These potential effects of the SGS models indicate that for LES to reproduce a resolvable-scale statistics, all the relevant conditional SGS stress, flux, and SGS production rates must be correctly predicted. An example in which this condition is not satisfied is the poor prediction of the conditional τ_{33} by the Smagorinsky model, which can lead to incorrect predictions of the conditional P_{F3} and hence the resolvable-scale vertical scalar flux even when F_3 is quite well predicted. Previous efforts to improve SGS models generally focused on the model predictions of the SGS stress and flux. The results here show that the predictions of the SGS production rates must also be improved.

4. *conclusion*

In the present study, we use field measurements data in a convective atmospheric boundary layer to analyze the subgrid-scale turbulence. The necessary conditions for LES correctly predict the resolvable-scale velocity-scalar JPDF are that the SGS models reproduce the conditional means of the SGS stress, the SGS stress production rate, the SGS scalar flux, the SGS scalar flux production rate, and the SGS scalar variance production rate conditional on the resolvable-scale velocity and scalar.

The results show that the conditional SGS scalar flux, its production rate, and the SGS scalar variance production rate depend strongly on the resolvable-scale velocity and scalar. The dependences are generally strong for positive temperature fluctuations and are weak for negative temperature fluctuations.

Analyses of the conditional SGS scalar flux and its production rate show that they are closely related to the surface layer dynamics and flow history. For positive θ^r fluctuations, eddies associated with updrafts generally come from the near ground region, which contain large magnitudes of vertical SGS flux and SGS stress, and experience strong shear and vertical temperature gradient, resulting in large SGS flux production rates. For small θ^r fluctuations, eddies are generally well mixed, therefore, the results tend to be more symmetric with respect to u_3^r. For negative θ^r fluctuations, eddies associated with downdrafts generally come from the mixed layer region, which carry relatively small fluxes, resulting small magnitudes and weak dependences of the conditional SGS scalar flux production rates on the resolvable-scale velocity. The vertical SGS scalar flux is shown to have a “slow” effect on the horizontal SGS scalar production rate. The horizontal SGS scalar flux does not influence directly the vertical SGS scalar flux production rate but nonetheless affects the resolvable-scale scalar PDF.

The conditional SGS scalar flux and the conditional SGS scalar flux production rate have similar trends and are generally well aligned with the alignment angle being generally less than 10°. This is consistent with the balance between the production rate and pressure destruction and the validity of using the SGS scalar flux and a time scale for the pressure destruction. The similarities and the dynamic connections between the conditional scalar flux and its production rate provide the potential of using the conditional scalar flux production rate to model the scalar flux in convective ABLs.

The trends of the SGS stress and its production rate for positive temperature fluctuations are similar to the results without conditioning on the resolvable-scale temperature fluctuations. The dependences are weak for negative temperature fluctuations. We argue that the dependences of the SGS stress and its production rate on the resolvable-scale temperature fluctuations are partly due to the flow history effect.

The Lumley triangle for the conditional SGS stress shows that the anisotropy of $\langle \tau_{ij} | u_1^r, u_3^r, \theta^r \rangle$ for positive temperature fluctuations is quite strong and is close to the that for $\langle \tau_{ij} | u_1^r, u_3^r \rangle$ (without conditioning on θ^r). The conditional SGS stress are not far from being axisymmetric with either one small or large eigenvalue. For small θ^r fluctuations, the results are somewhat similar to the results for positive θ^r fluctuations. For negative θ^r fluctuations, the conditional SGS stress is less anisotropic.

The conditional SGS stress and its production are generally well aligned for positive θ^r fluctuations and are less well aligned for negative θ^r, consistent with the results on the Lumley triangle and the possible quasi-equilibrium between the SGS stress production and pressure destruction.

Our statistical *a priori* test show that the Smagorinsky model underpredicts the conditional horizontal scalar flux, because the small magnitude of the horizontal scalar gradients. It predicts well the conditional vertical SGS scalar flux because it uses the dominant vertical scalar gradients.

The Smagorinsky model can also predict well the trends of the conditional horizontal scalar flux production rate, because the conditional τ_{13} and F_3 are quite well predicted. However, it predicts poorly the conditional vertical SGS scalar flux production rate due to its poor prediction of τ_{33}. The conditional scalar variance production rate are well predicted because the trend of F_3 is well predicted.

The nonlinear model can predict well the conditional horizontal SGS scalar flux. Both the conditional horizontal and vertical SGS scalar flux production rates are underpredicted. Predictions of the SGS flux using the nonlinear model are found to be closely related to predictions using the Smagorinsky model and the quasi-equilibrium between the production and pressure destruction. The analysis of the nonlinear model using the Smagorinsky model and the surface layer dynamics provides a physical explanation of the performance of the nonlinear model. A similar analyse of the nonlinear SGS stress model are also performed.

The dependences of the SGS stress and its production rate on the resolvable-scale temperature suggest that it may be beneficial to model such dependences to account for flow-history effects. Analyses of the SGS models show that the current SGS models have varying level of performance in predicting different SGS components. Often the poor model prediction of one SGS component affects the prediction of the production rate of another component, thereby resulting in errors in the LES statistics that depend on the production rate. Therefore, efforts to improve SGS models should be focused on the correct predictions of all the relevant SGS variables related to the LES statistics of interests or of importance to the intended applications.

We thank Drs. Tom Horst, Don Lenschow, Chin-Hoh Moeng, Peter Sullivan, and Jeff Weil at NCAR for conducting the field campaign of the HATS collaboration and for providing the data. We also thank Professor John C. Wyngaard for valuable discussions. This work was supported by the National Science Foundation through grant No. ATM-0222421.

References

Bardina, J., J. H. Ferziger and W. C. Reynolds (1980). Improved subgrid scale models for large eddy simulation. *AIAA Paper 80-1357*.

Borue, V. and S. Orszag (1998). Local energy flux and subgrid-scale statistics in three-dimensional turbulence. *J. Fluid Mech.* **366**, 1–31.

Cerutti, S., C. Meneveau and O. M. Knio (2000). Spectral and hyper eddy viscosity in high-reynolds-number turbulence. *J. Fluid Mech.* **421**, 307–338.

Chen, Q. and C. Tong (2006). Investigation of the subgrid-scale stress and its production rate in a convective atmospheric boundary layer using measurement data. *J. Fluid Mech.* **547**, 65 – 104.

Chen, Q., D. Wang, H. Zhang and C. Tong (2005). Effects of subgrid-scale turbulence on resolvable-scale velocity-scalar statistics. *J. Turbulence* **6**, 36.

Chen, Q., H. Zhang, D. Wang and C. Tong (2003). Subgrid-scale stress and its production rate: conditions for the resolvable-scale velocity probability density function. *J. Turbulence* **4**, 027.

Clark, R. A., J. H. Ferziger and W. C. Reynolds (1979). Evaluation of subgrid-models using an accurately simulated turbulent flow. *J. Fluid Mech.* **91**, 1–16.

Domaradzki, J. A., W. Liu and M. E. Brachet (1993). An analysis of subgrid-scale interactions in numerically simulated isotropic turbulence. *Phys. Fluids A* **5**, 1747 – 1759.

Edsall, R. M., D. W. Thomson, J. C. Wyngaard and L. J. Peltier (1995). A technique for measurement of resolvable-scale flux budgets. In: *11th Symp. on Boundary Layers and Turbulence*. pp. 15 – 17. Amer. Meteor. Soc.. Charlotte, NC.

Härtel, C., L. Kleiser, F. Unger and R. Friedrich (1994). Subgrid-scale energy-transfer in the near-wall region of turbulent flow. *Phys. Fluid* **6**, 3130 – 3143.

Horst, T. W., J. Kleissl, D. H. Lenschow, C. Meneveau, C.-H. Moeng, M. B. Parlange, P. P. Sullivan and J. C. Weil (2004). Hats: Field observations to obtain spatially-filtered turbulence fields from transverse arrays of sonic anemometers in the atmosperic surface flux layer. *J. Atmos. Sci.* **61**, 1566 – 1581.

Jaberi, F. A., R. S. Miller and P. Givi (1996). Conditional statistics in turbulent scalar mixing and reaction. *AIChE J.* **42**, 1149–1152.

Juneja, A. and J. G. Brasseur (1999). Characteristics of subgrid-resolved-scale dynamics in anisotropic turbulence, with application to rough-wall boundary layers. *Phys. Fluid* **11**, 3054 – 3068.

Kaimal, J. C., J. C. Wyngaard, Y Izumi and O. R. Coté (1972). Spectral characteristic of surface-layer turbulence. *Q.J.R. Met. Soc.* **98**, 563 – 589.

Kleissl, J., C. Meneveau and M. Parlange (2003). On the magnitude and variability of subgrid-scale eddy-diffusion coefficients in the atmospheric surface layer. *J. Atmos. Sci.* **60**, 2372 – 2388.

Leonard, A. (1974). Energy cascade in large-eddy simulations of turbulent fluid flows.. *Adv. in Geophys.* **18**, 237 – 248.

Lilly, D. K. (1967). The representation of small-scale turbulence in numerical simulation experiments. *In Proc. IBM Scientific Computing Symp. Environ. Sci.* p. 195.

Liu, S., C. Meneveau and J. Katz (1994). On the properties of similarity subgrid-scale models as deduced from measurements in a turbulent jet. *J. Fluid Mech.* **275**, 83–119.

Lumley, J. L. (1965). Interpretation of time spectra measured in high-intensity shear flows. *Phys. Fluids* **6**, 1056 – 1062.

Lumley, J. L. (1978). Computational modeling of turbulent flows. *Adv. Appl. Mech.* **18**, 123 – 176.

Lund, T. S. and E. A. Novikov (1992). Parametrization of subgrid-scale stress by the velocity gradient tensor. *Annual Research Briefs - Center for Turbulence Research* pp. 27 – 43.

Mason, P. J. (1994). Large-eddy simulation: A critical review of the technique. *Quart. J. Roy. Meteor. Soc.* **120**, 1–26.

Mason, P. J. and D. J. Thomson (1992). Stochastic backscatter in large-eddy simulation of boundary layers. *J. Fluid. Mech.* **242**, 51 – 78.

McMillan, O. J. and J. H. Ferziger (1979). Direct testing of subgrid-scale models. *Am. Inst. Aeronaut. Astronaut. J.* **17**, 1340 – 1346.

Meneveau, C. (1994). Statistics of turbulence subgrid-scale stress: Necessary conditions and experimental tests. *Phys. Fluids* **6**, 815.

Nieuwstadt, F. T. M. and P. J. P. M. M. de Valk (1987). A large eddy simulation of of buoyant and non-buoyant plume dispersion in the atmospheric boundary layer. *Atmos. Environ.* **21**, 2573 – 2587.

Peltier, L. J., J. C. Wyngaard, S. Khanna and J. Brasseur (1996). Spectra in the unstable surface layer. *J. Atmos. Sci.* **53**, 49 – 61.

Piomelli, U. (1993). High reynolds-number calculations using the dynamic subgrid-scale stress model. *Phys. Fluid A* **5**, 1484 – 1490.

Piomelli, U., P. Moin and J. H. Ferziger (1988). Model consistency in large eddy simulation of turbulent channel flows. *Phys. Fluid* **31**, 1884 – 1891.

Pope, S. B. (2000). *Turbulent Flows*. Cambridge University press. Cambridge, England.

Porté-Agel, F., M. B. Parlange, C. Meneveau and W. E. Eichinger (2001). A priori field study of the subgrid-scale heat fluxes and dissipation in the atmospheric surface layer. *J. Atmos. Sci.* **58**, 2673–2698.

Rajagopalan, A. G. and C. Tong (2003). Experimental investigation of scalar-scalar-dissipation filtered joint density function and its transport equation. *Phys. Fluids* **15**, 227–244.

Sabelnikov, V. A. (1998). Asymptotic solution of the equation for the probability distribution of a passive scalar in grid turbulence with a uniform mean scalar gradient. *Phys. Fluids* **10**, 753 – 755.

Sarghini, F., U. Piomelli and E. Balaras (1999). Scale-similar models for large-eddy simulations. *Phys. Fluids* **11**, 1596–1607.

Smagorinsky, J. (1963). General circulation experiments with the primitive equations: I. the basic equations. *Mon. Weather Rev.* **91**, 99 – 164.

Sullivan, P. P., J. C. McWilliams and C.-H. Moeng (1994). A subgrid-scale model for large-eddy simulation of planetary boundary-layer flows. *Boundary-Layer Met.* **71**, 247 – 276.

Sullivan, P. P., T. W. Horst, D. H. Lenschow, C.-H. Moeng and J. C. Weil (2003). Structure of subfilter-scale fluxes in the atmospheric surface layer with application to large-eddy simulation modeling. *J. Fluid Mech.* **482**, 101 – 139.

Tao, B., J. Katz and C. Meneveau (2000). Geometry and scale relationships in high reynolds number turbulence determined from three-dimensional holographic velocimetry. *Phys. Fluids* **12**, 941 – 944.

Tong, C. (2001). Measurements of conserved scalar filtered density function in a turbulent jet. *Phys. Fluids* **13**, 2923–2937.

Tong, C., J. C. Wyngaard and J. G. Brasseur (1999). Experimental study of subgrid-scale stress in the atmospheric surface layer. *J. Atmos. Sci.* **56**, 2277–2292.

Tong, C., J. C. Wyngaard, S. Khanna and J. G. Brasseur (1997). Resolvable- and subgrid-scale measurement in the atmospheric surface layer. In: *12th Symp. on Boundary Layers and Turbulence*. pp. 221 – 222. Amer. Meteor. Soc.. Vancouver, BC, Canada.

Tong, C., J. C. Wyngaard, S. Khanna and J. G. Brasseur (1998). Resolvable- and subgrid-scale measurement in the atmospheric surface layer: technique and issues. *J. Atmos. Sci.* **55**, 3114–3126.

Wang, D. and C. Tong (2002). Conditionally filtered scalar dissipation, scalar diffusion, and velocity in a turbulent jet. *Phys. Fluids* **14**, 2170–2185.

Wang, D., C. Tong and S. B. Pope (2004). Experimental study of velocity filtered joint density function and its transport equation. *Phys. Fluids* **16**, 3599 – 3613.

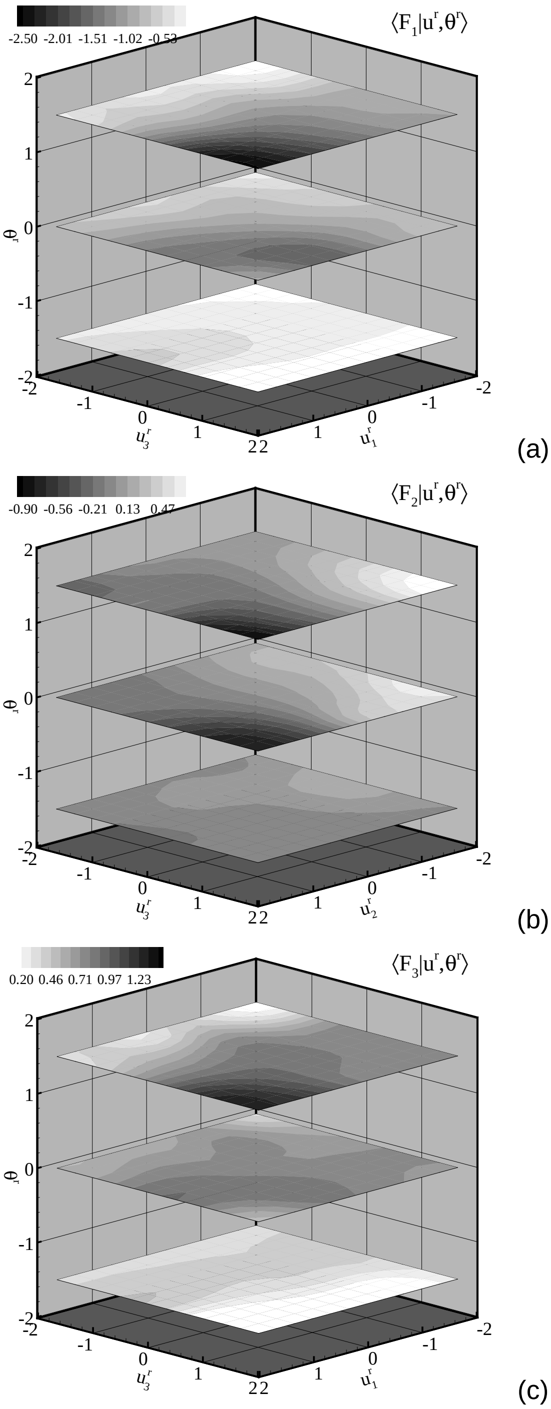

Figure 2: Conditional means of the SGS scalar flux. The dependences on resolvable-scale velocity are strong for positive θ^r and are weak for negative θ^r.

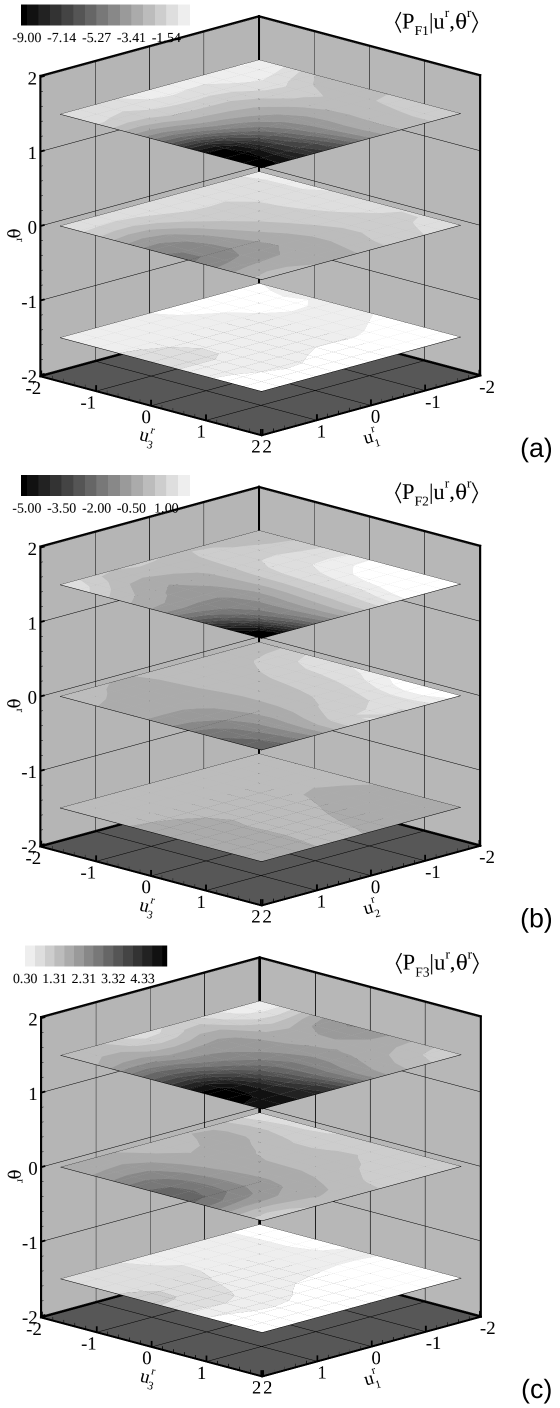

Figure 3: Conditional means of the SGS scalar flux production rate.

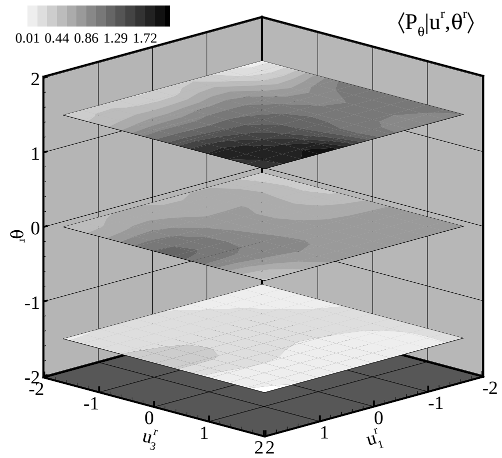

Figure 4: Conditional mean of the SGS scalar variance production rate.

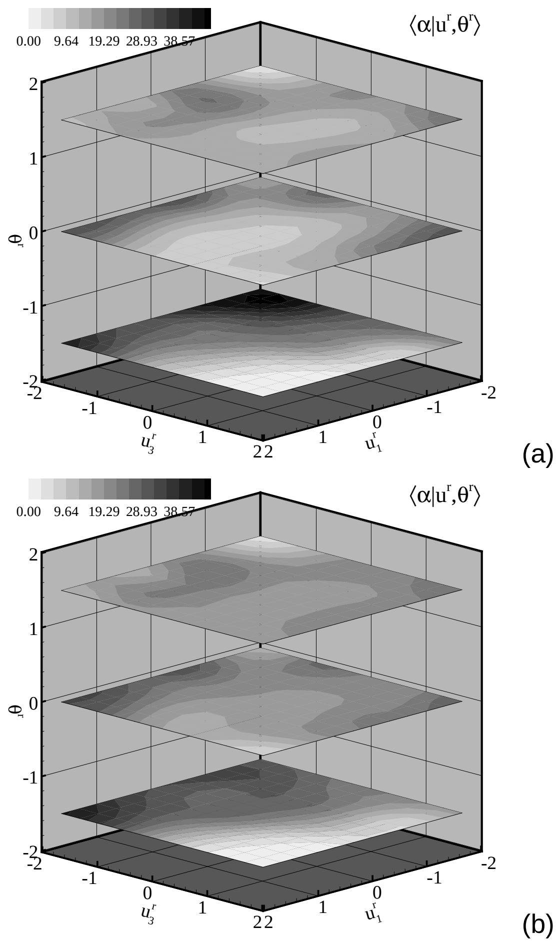

Figure 5: Geometric alignment of the measured conditional SGS scalar flux and the conditional SGS stress production rate. (a), the alignment angles are small for positive u_3^r and θ^r and increases for negative u_3^r and θ^r; (b), the effects of buoyancy is included, and the alignment angles are similar to (a).

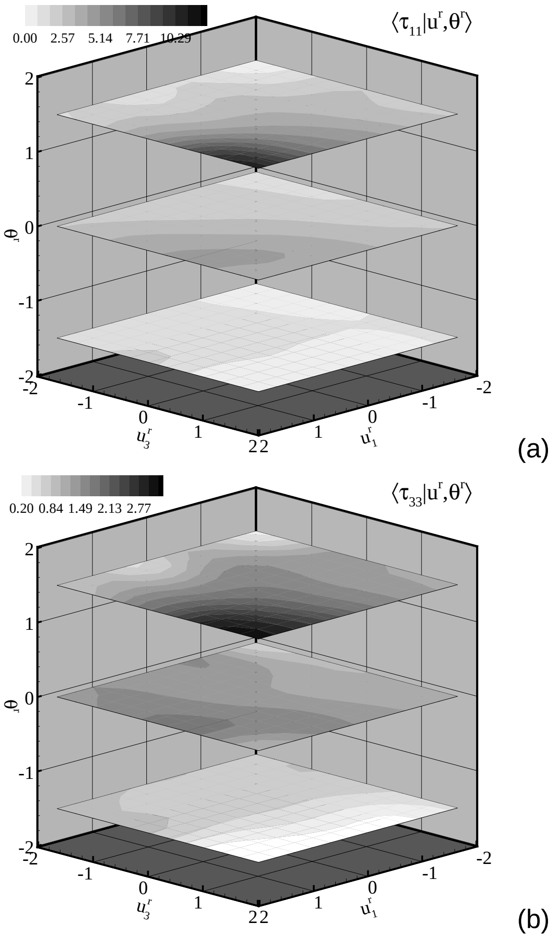

Figure 6: Conditional means of the normal components of the SGS stress. The dependences are strong for positive θ^r and are weak for negative θ^r.

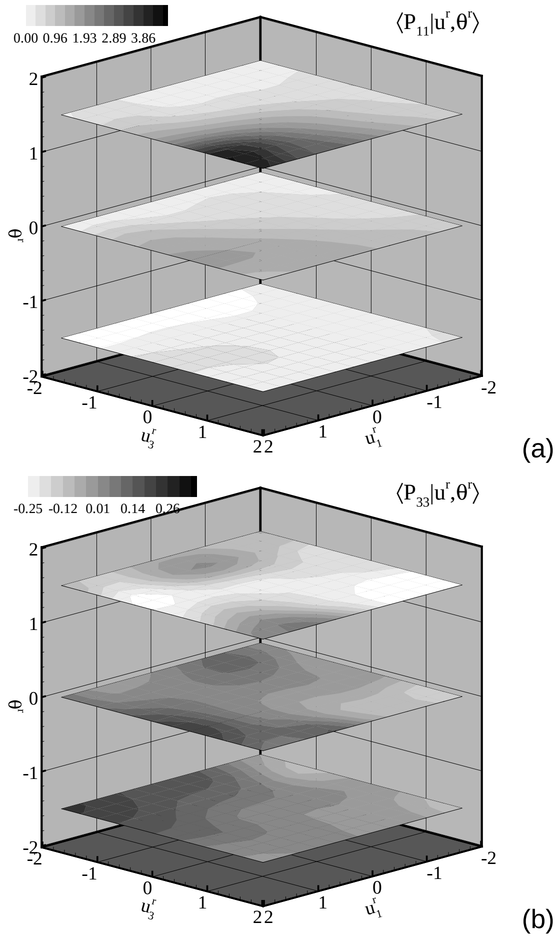

Figure 7: Conditional means of the normal components of the SGS stress production rates.

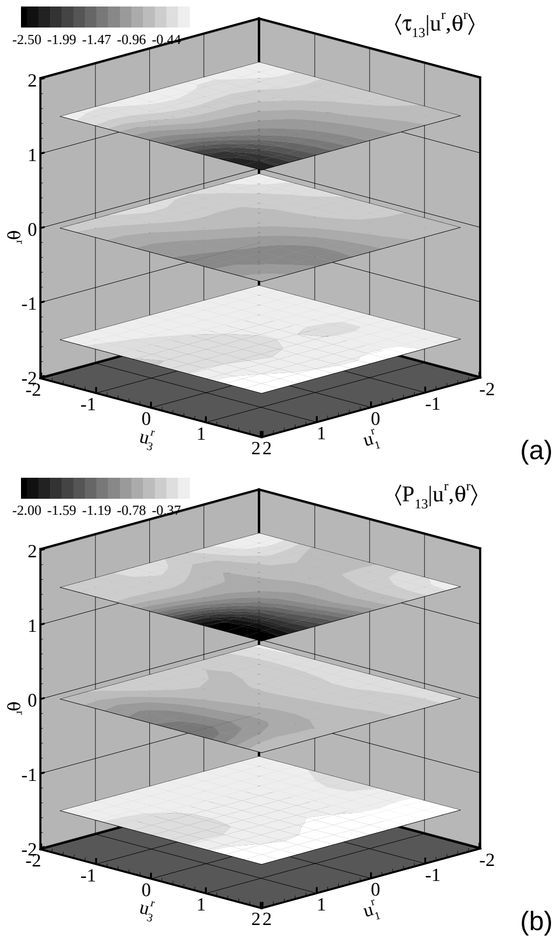

Figure 8: Conditional means of the shear components of the SGS stress and the shear production rate.

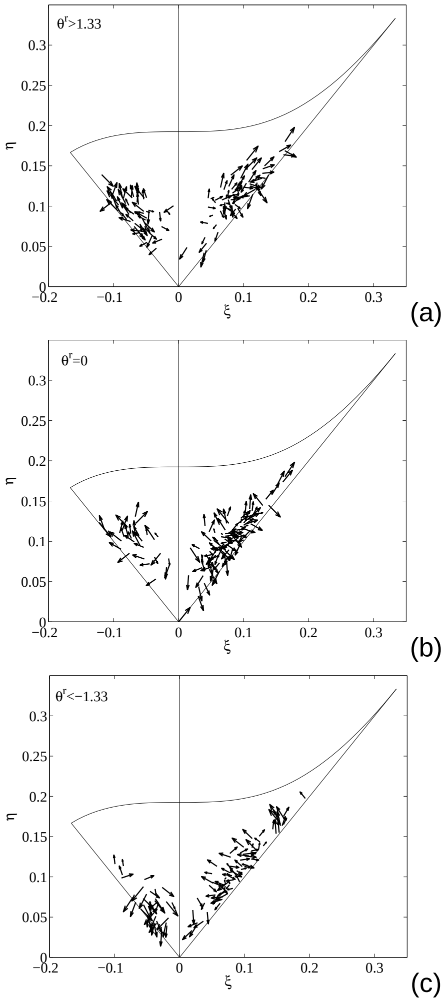

Figure 9: Lumley triangle representation of the conditional SGS stress. The arrows represent the conditional vector (u_1^r, u_3^r). (a), for positive θ^r, $\langle \tau_{ij}|u_1^r, u_3^r, \theta^r\rangle$ is quite anisotropic and close to the results for $\langle \tau_{ij}|u_1^r, u_3^r\rangle$ (without conditioning on θ^r); (b), for small θ^r, the results are similar to the (a); (c), for negative θ^r, the conditional SGS stress is less anisotropy.

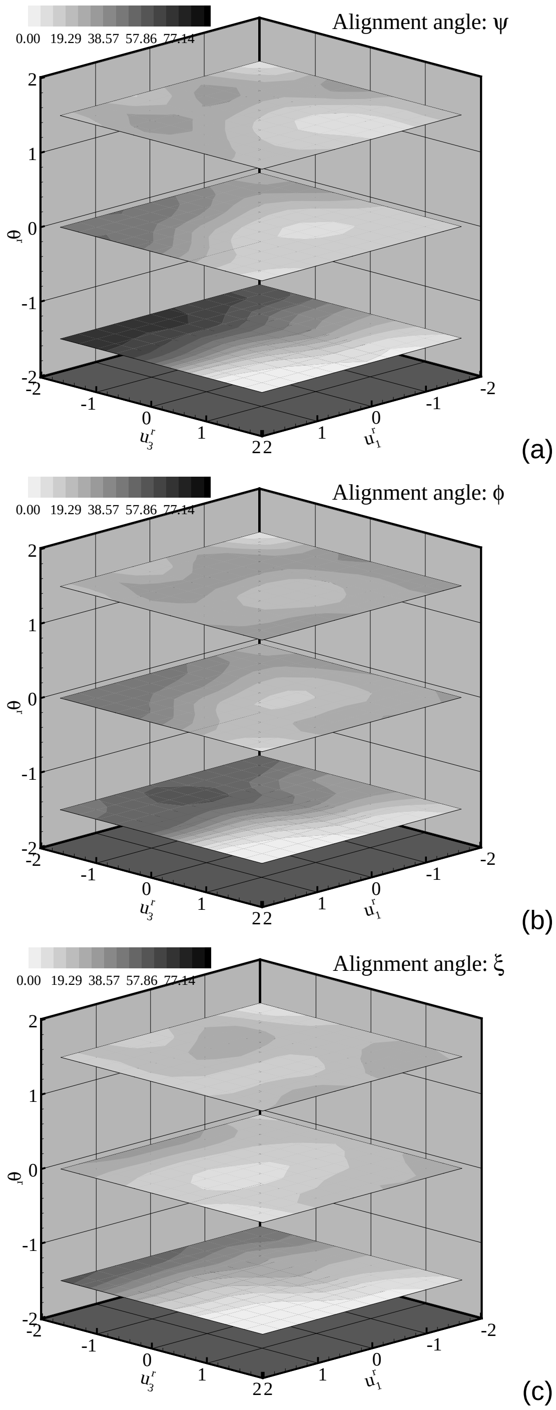

Figure 10: Geometric alignment of conditional SGS stress and its production rate. The alignment angles are small for positive θ^r and increases for negative θ^r and u_3^r.

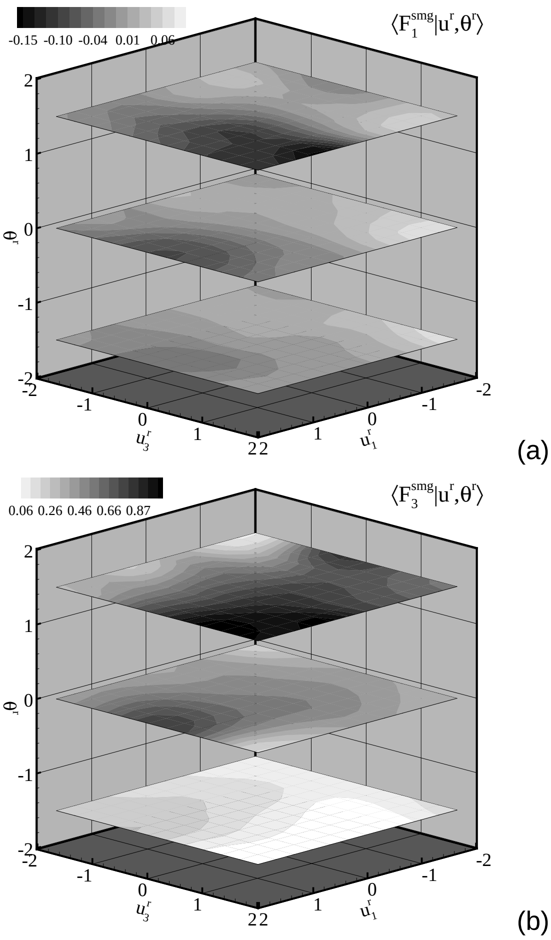

Figure 11: Predicted conditional SGS scalar flux using the Smagorinsky model. The trend of $\langle F_3|\mathbf{u}^r,\theta^r\rangle$ is well predicted.

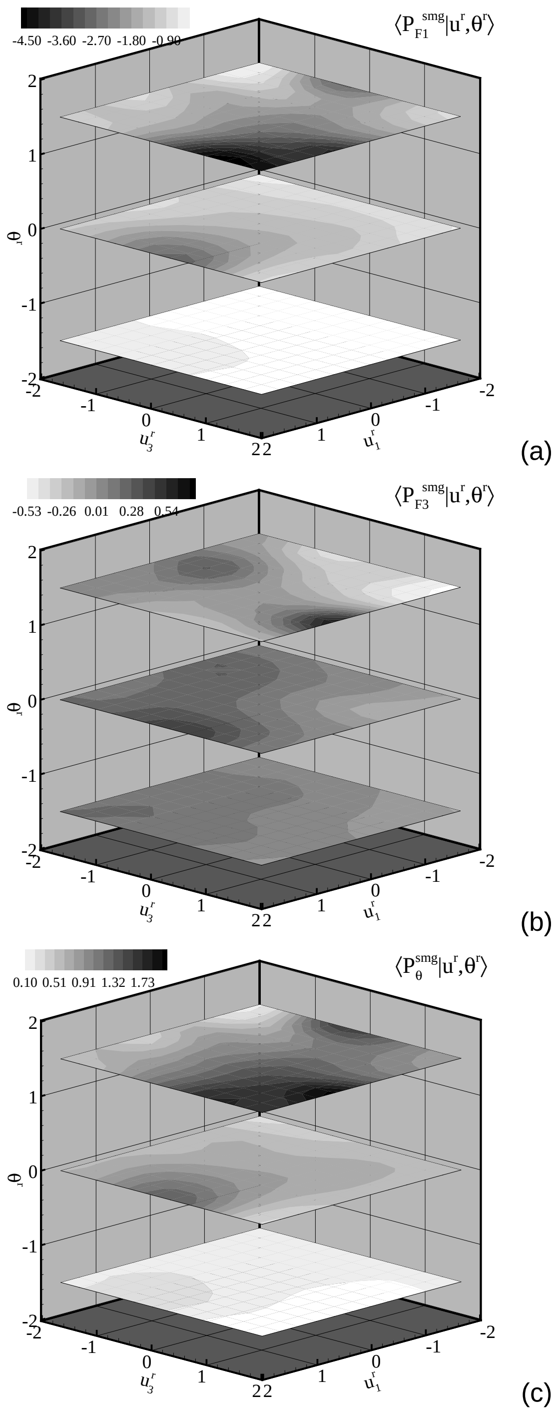

Figure 12: Predicted conditional SGS scalar flux production rate and SGS scalar variance production rate using the Smagorinsky model. The trend of $\langle P_{F1}|\mathbf{u}^r, \theta^r\rangle$ is well predicted.

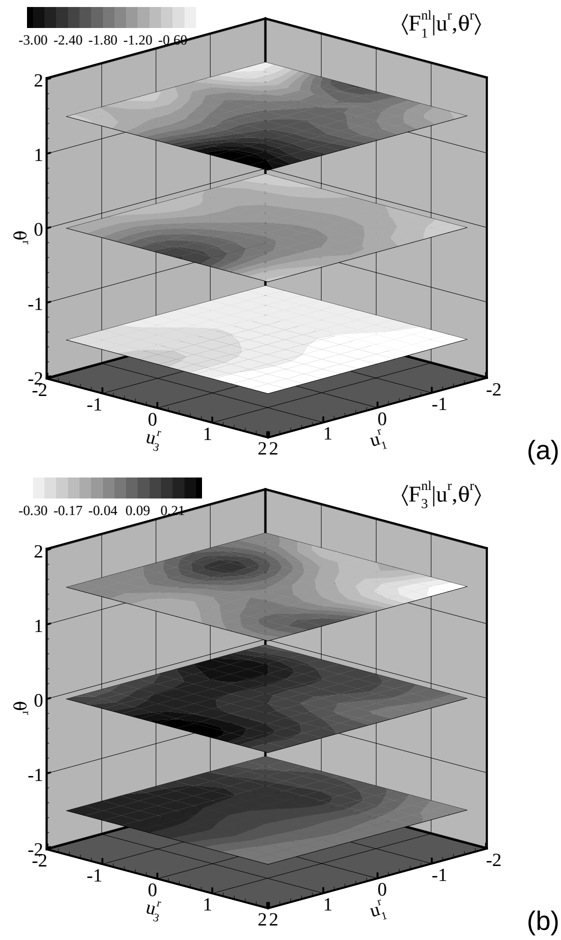

Figure 13: Predicted conditional SGS scalar flux using the nonlinear model. The trend of $\langle F_1|\mathbf{u}^r, \theta^r\rangle$ is well predicted.

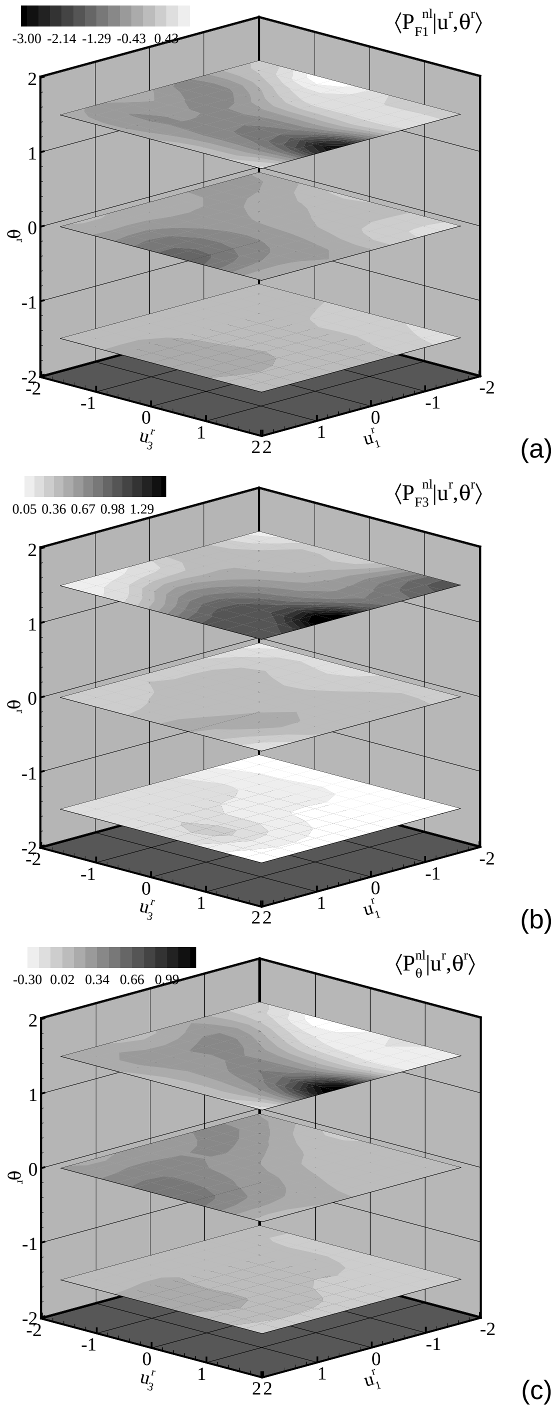

Figure 14: Predicted conditional SGS scalar flux production rate and the scalar variance production rate using the nonlinear model.

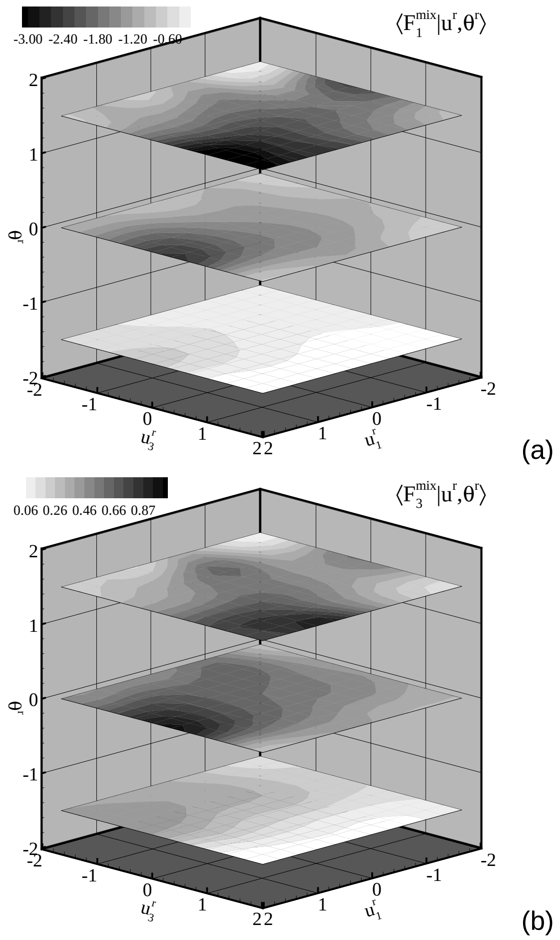

Figure 15: Predicted conditional SGS scalar flux using the mixed model.

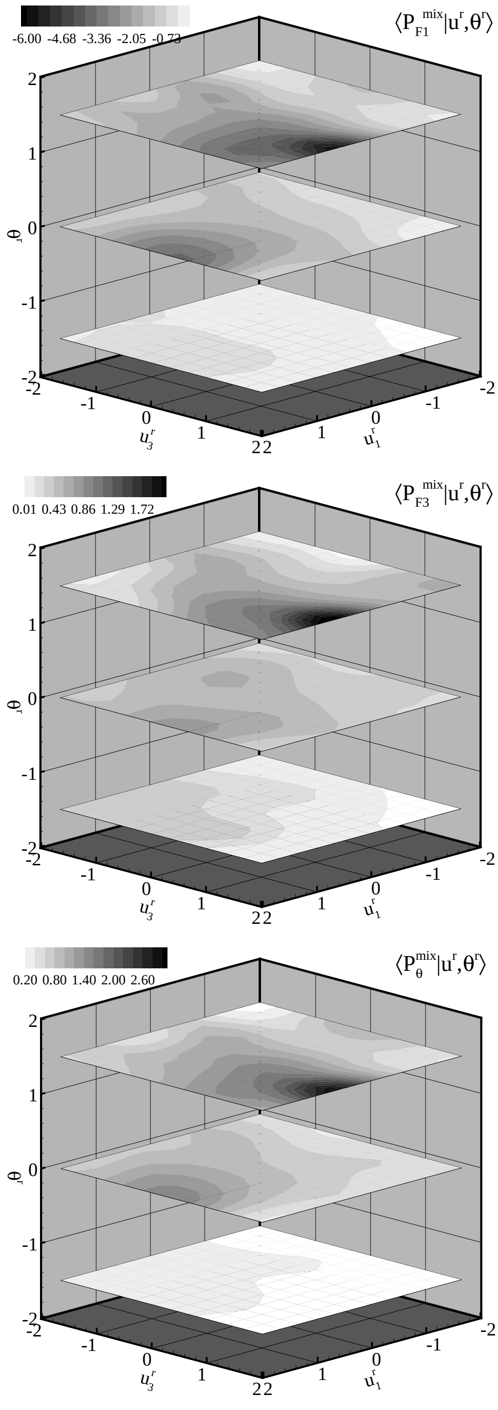

(a)

(b)

(c)

Figure 16: Predicted conditional SGS scalar flux production rate and SGS scalar variance production rate using the mixed model.